BNL-104271-2014-JA

AGU PUBLICATIONS

JGR

Journal of Geophysical Research: Atmospheres

RESEARCH ARTICLE
10.1002/2013JD019813

Special Section:
Fast Physics in Climate Models: Parameterization, Evaluation and Observation

Key Points:
- Large differences in the means of decade-long cloud fractions
- Different cloud fraction estimates show different tendencies of increase
- Cloud fractions at different scales have different distributions

Correspondence to:
W. Wu,
wwu@bnl.gov

Citation:
Wu, W., Y. Liu, M. P. Jensen, T. Toto, M. J. Foster, and C. N. Long (2014), A comparison of multiscale variations of decade-long cloud fractions from six different platforms over the Southern Great Plains in the United States, *J. Geophys. Res. Atmos.*, *119*, 3438–3459, doi:10.1002/2013JD019813.

Received 7 MAR 2013
Accepted 5 MAR 2014
Accepted article online 10 MAR 2014
Published online 28 MAR 2014

A comparison of multiscale variations of decade-long cloud fractions from six different platforms over the Southern Great Plains in the United States

Wei Wu[1], Yangang Liu[1], Michael P. Jensen[1], Tami Toto[1], Michael J. Foster[2], and Charles N. Long[3]

[1]Atmospheric Sciences Division, Brookhaven National Laboratory, Upton, New York, USA, [2]Cooperative Institute for Meteorological Satellite Studies, University of Wisconsin, Madison, Wisconsin, USA, [3]Pacific Northwest National Laboratory, Richland, Washington, USA

Abstract This study compares 1997–2011 observationally based cloud fraction estimates from six different platforms (three ground-based estimates and three satellite-based estimates) over the Southern Great Plains, United States. The comparisons are performed at multiple temporal and spatial scales. The results show that 1997–2011 mean cloud fractions from the Active Remote Sensing of CLouds (ARSCL) and from the International Satellite Cloud Climatology Project (ISCCP) are significantly (at a 2% significance level, two-sided *t* test) larger than the others, having 0.08 and 0.15 larger mean diurnal variations, 0.08 and 0.13 larger mean annual variations, and 0.08 and 0.14 larger interannual variations, respectively. Although more high (low) clouds are likely a reason for larger ARSCL (ISCCP) cloud fractions, other mechanisms cannot be ruled out and require further investigations. Furthermore, half of the estimates exhibit a significant (at a 1% significance level, one-sided *t* test) overall increase of 0.08–0.10 in the annually averaged cloud fractions from 1998 to 2009; another half of the estimates exhibit little tendency of increase in this decade. Monthly cloud fractions from all the estimates exhibit quasi-Gaussian frequency distributions while the distributions of daily cloud fractions are found dependent on spatial scales. Cloud fractions from all the estimates show much larger seasonal variations than diurnal variations. Findings from this study suggest caution when using observationally based cloud fraction estimates for climate studies such as evaluating model performance and reinforce the need of consistency in defining and retrieving cloud fractions.

1. Introduction

Cloud fraction (amount) is known to be an important factor in modulating the Earth's radiation budget [e.g., *Wielicki et al*., 2002; *Loeb et al*., 2007; *Bender*, 2011; *Liu et al*., 2011]. In climate models, cloud fraction is one of the major parameters in calculation of cloud radiation-precipitation interactions [e.g., *Manabe and Strickler*, 1964; *Ramanathan and Coakley*, 1978; *Slingo et al*., 1989; *Sundqvist et al*., 1989; *Smith*, 1990; *Tiedtke*, 1993; *Del Genio et al*., 1996; *Park and Bretherton*, 2009; *Sokolov and Monier*, 2012]. For understanding current climate change and predicting future climate variability, observationally based cloud fraction estimates have been intensively studied for decades [e.g., *Minnis*, 1989; *Wielicki and Parker*, 1992; *Di Girolamo and Davies*, 1997; *Rossow and Schiffer*, 1999; *Clothiaux et al*., 2000; *Hogan et al*., 2001; *Kassianov et al*., 2005; *Long et al*., 2006a; *Min et al*., 2008; *Ackerman et al*., 2008]. Cloud fraction products retrieved from observations have been widely used in evaluation of model performance [e.g., *Jakob*, 1999; *Guichard et al*., 2003; *Bedacht et al*., 2007; *Wilkinson et al*., 2008; *Walsh et al*., 2009; *Ahlgrimm and Köhler*, 2010; *Bouniol et al*., 2010; *Kennedy et al*., 2011; *Wu et al*., 2012; *Xie et al*., 2013].

Before quantitatively comparing different observationally based cloud fraction estimates, it is necessary to understand how cloud fraction is defined. Unfortunately, "cloud fraction" or even "a cloud" is not a well-defined quantity. According to the American Meteorological Society Glossary (http://glossary.ametsoc.org/), a cloud is defined as "a visible aggregate of minute water droplets and/or ice particles in the atmosphere above the Earth's surface," and cloud fraction is defined as "the amount of sky estimated to be covered by a specified cloud type or level (partial cloud fraction) or by all cloud types and levels (total cloud fraction)." Apparently, the determination of whether or not a cloud is present or what fraction of the sky is covered by a cloud is dependent on the observer or on the characteristics of the instrument that is used to make the observations. In reality, there exist various definitions of cloud fraction, mainly because of the differences in observational

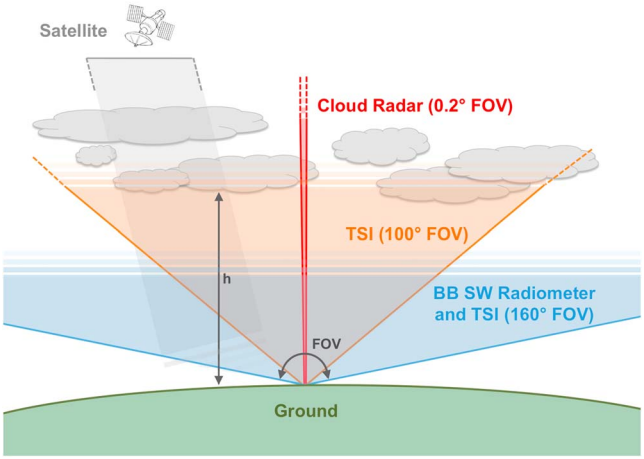

Figure 1. A sketch, illustrating various instrumental FOVs associated with several different cloud fraction definitions. "BB SW radiometer" refers to "broadband shortwave radiometer." For a cloud base height of h, the horizontal sky area seen by a surface instrument equals $\tan^2\left(\frac{\mathrm{FOV}}{2}\right)\pi h^2$. Different satellites (e.g., geostationary and polar orbiting) over the Southern Great Plains (SGP) site in general have different view zenith angles which are referenced to nadir from the Earth's surface [*Yi et al.*, 2001].

instruments, retrieval methods, or model parameterizations used to determine this quantity. Discussions on cloud fraction and its important role on determining the Earth's radiation budget can be found in numerous papers. Among them, a thorough and down-to-earth discussion on cloud fraction was given by *Wiscombe* [2005]. One relevant key point addressed by *Wiscombe* [2005] is that the determination of cloud fraction depends on wavelength. In other words, instruments or a threshold of radiation properties (dependent on wavelength) used to determine a cloud could affect the final products of cloud fraction. As will be discussed later in this paper, the determination of cloud fraction also depends on many other factors including cloud orientation and morphology, and instrumental viewing geometry and field of view (FOV). Nevertheless, a detailed investigation on causes of the differences in determination of cloud fraction is beyond the scope of this paper, and the subject of future research.

Besides the visual observation of cloud cover [*Warren et al.*, 2007], a number of remote-sensing approaches have been developed over the years to retrieve cloud fraction estimates. For example, the "total cloud fraction" (cloud fraction hereafter) retrieved from ground-based passive radiometric observations represents the effective 160° FOV hemispheric fractional sky cover from a surface point at a particular time [e.g., *Long et al.*, 2006a]. The cloud fraction retrieved from ground-based sky color images is a hemispheric view from a surface point similar to the radiometrically retrieved sky cover, and as in the case of the Atmospheric Radiation Measurement (ARM) Program [*Stokes and Schwartz*, 1994; *Ackerman and Stokes*, 2003] sky imager processing is also restricted to a 160° FOV [e.g., *Long et al.*, 2001, 2006b]. The ARM observations also include a 100° FOV cloud fraction retrieval from the sky images which are used in this study. As shown in *Kassianov et al.* [2005], 15 min or longer averages of highly sampled (1 min resolution) 100° FOV sky images can effectively represent nadir-projected cloud fraction and virtually eliminate retrieval errors associated with circumsolar brightness and near-horizon areas in the sky images [*Long*, 2010]. The cloud fraction from a vertically upward pointing active remote sensing (i.e., radars and lidars) instruments represents the number of occurrences of cloudy observations in a narrow "pencil beam" overhead divided by the total number of observations within a particular time interval [e.g., *Clothiaux et al.*, 2000; *Kollias et al.*, 2005]. The cloud fraction from satellite observations represents the number of "cloudy" pixels, usually determined by comparing to clear-sky thresholds, divided by the total number of pixels [e.g., *Zuidema and Hartmann*, 1995; *Ackerman et al.*, 2008]. Figure 1 illustrates the various instrumental FOVs associated with several different cloud fraction definitions. The evident differences in the observational FOVs and corresponding instrument sensitivities are expected to cause differences in the resulting cloud fraction estimates, which could lead to confusion in cloud fraction applications.

In large-scale climate models, such as general circulation models (GCMs), the representation of cloud fraction is parameterized either by area or by volume. Although the cloud fraction calculated as the ratio of the total volume of cloud to the total volume of the model grid box is always smaller than that calculated as the ratio of horizontally projected area of cloud to the area of the model grid box, they can be related mathematically [*Brooks et al.*, 2005]. Further, the nadir-view cloud fraction, i.e., the horizontal area fraction covered by clouds viewed from nadir as parameterized in climate models [e.g., *Del Genio et al.*, 1996], is dependent on assumptions about the overlap of cloud fraction in layers within a single-model column [e.g., *Barker et al.*, 1999; *Hogan and*

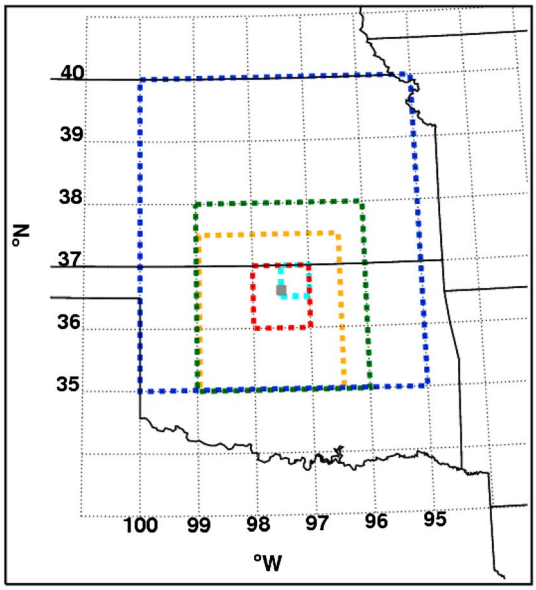

Figure 2. The geographic locations and grid sizes of the observationally based cloud fraction estimates investigated in this study. The gray solid box represents the SGP Central Facility. The boxes outlined by colored dashed lines represent spatial scales at the following: (1) 0.5° latitude/longitude (cyan, for GOES), (2) 1° latitude/longitude (red, for GOES and PATMOS-x), (3) 2.5° equal area (orange, for ISCCP D1), (4) 3° latitude/longitude (green, for GOES and PATMOS-x), and (5) 5° latitude/longitude (blue, for GOES, PATMOS-x, ISCCP D1, and ISCCP D2).

Illingworth, 2000; *Mace and Benson-Troth*, 2002]. Although this nadir-view cloud fraction was almost unbiased compared to FOV ≤ 100° fractional sky cover as mentioned above, it was found to always be smaller than ground-based 15 min averages of 160° FOV fractional sky cover [*Kassianov et al.*, 2005]. The differences of cloud fraction representations among different climate models and between climate models and observations pose an additional challenge in evaluating modeled cloud fractions.

Although there are numerous studies on evaluation of modeling clouds or cloud impacts on atmospheric radiation, systematic investigations on comparison of multiscale long-term mean cloud fraction using ground- and satellite-based cloud fraction estimates are rare. The objective of this paper is to compare decade-long cloud fraction statistics at multiple spatial and temporal scales using high-resolution cloud fraction estimates from six different platforms over the Southern Great Plains (SGP) in Oklahoma, United States. Statistical frequency distributions of daily and monthly cloud fractions are also compared. Statistical significances of the differences between the means and variances of different cloud fraction estimates are examined. We also provide examples to illustrate potential causes of large cloud fraction differences. Section 2 briefly introduces data and approaches. Section 3 shows results. Sections 4 and 5 are discussions and summary.

2. Data and Approaches

2.1. Data

In this study, we compare 1997–2011 observationally based cloud fraction estimates from three ground-based estimates and three satellite-based estimates over the ARM SGP Central Facility (97.485°W, 36.605°N), located in north-central Oklahoma, United States. The three ground-based estimates are from the following: (1) the Active Remote Sensing of CLouds (ARSCL) value-added product, (2) the Total Sky Imager (TSI), and (3) the Radiative Flux Analysis (RFA) based on the Solar and Infrared Radiation System. The three satellite-based estimates are from the following: (1) the Geostationary Operational Environmental Satellite (GOES), (2) the International Satellite Cloud Climatology Project (ISCCP), and (3) the Advanced Very High Resolution Radiometer (AVHRR) Pathfinder Atmospheres Extended (PATMOS-x). Figure 2 presents the geographic location and grid sizes of the cloud fraction estimates investigated in this study.

2.1.1. Cloud Fraction Estimates From Ground-Based Active Remote Sensing

The ARM SGP Central Facility includes a suite of vertically upward pointing narrow FOV active remote sensors that provide detailed observations of the distribution of clouds and hydrometeors within the overlying atmospheric column. These sensors include a 35 GHz millimeter wavelength cloud radar (MMCR) [*Moran et al.*, 1998], a micropulse lidar (MPL) [*Spinhurne*, 1993], and a laser ceilometer. None of these sensors can detect all cloud types under all conditions. The MMCR may miss thin clouds, particularly cirrus clouds and thin liquid-water clouds [*Turner et al.*, 2007], and cannot distinguish cloud boundaries from drizzle and heavier precipitation. The laser instruments cannot penetrate thick low-level clouds and therefore cannot detect cloud layers that lie above them. The MMCR has a 0.2° beam width which results in a horizontal resolution of 35 m at a height of 10 km. The MMCR cycles through a sequence of observing modes optimized for the observation of boundary layer clouds, cirrus clouds, and precipitating clouds [*Kollias et al.*, 2005, 2007a]. The

MPL and ceilometers are ground-based optical remote sensors that are mainly used for the determination of the lowest cloud base, particularly in precipitating conditions where the MMCR has difficulties distinguishing between cloud and precipitation particles, and the MPL is also used to supplement the detection of high clouds (when not blocked by lower clouds) that the MMCR cannot detect.

The MMCR observations are combined with the MPL and ceilometer observations to produce best estimate time-height profiles of hydrometeor locations, radar reflectivites, mean Doppler velocities, and Doppler spectral widths in the ARSCL value-added product [*Clothiaux et al*., 2000]. ARSCL provides these profiles based on sampling on a 10 s, 45 m vertical height interval grid. The cloud frequency of occurrence (cloud fraction hereafter) is estimated as the ratio of the number of 10 s time steps that contain detected clouds to the total number of time steps within a predetermined time window. This cloud frequency data set is determined by the ground-based active remote sensors and used to represent cloud fraction for comparisons in this study. We use hourly ARSCL total cloud fraction estimates from the ARM Best Estimate (ARMBE) value-added product [*Xie et al*., 2010] from January 1997 to December 2010. The hourly cloud fraction vertical profiles (based on MMCR and MPL) from the same data file are used to generate Figure 10. The data are available from November 1996 to January 2011 at http://www.arm.gov/sgpcmbe_cldrad_v2.2b_C1.c1. For inhomogeneous cloud cases such as broken clouds or near-cloud field boundaries, the frozen turbulence assumptions inherent in the conversion of cloud frequency of occurrence to cloud fraction may not hold.

2.1.2. Cloud Fraction Estimates From Ground-Based Hemispheric Observations

There are two separate cloud fraction estimates derived from ground-based hemispheric observations at the ARM SGP Central Facility. One is derived from the total sky imager measurements (TSI) and the other from broadband solar radiometer measurements (RFA).

The TSI captures 24 bit color images of the hemispheric view of the sky at 352×288 pixel resolution every 30 s. A cloud decision algorithm uses the ratio of red-to-blue pixel values to determine the presence of clouds over a vertically upward pointing 160° FOV, and also a smaller such as 100° FOV. A user-defined lower limit is set for the clear-sky red-to-blue ratio value, and any pixels for which the ratio exceeds this clear-sky limit are counted as cloudy. The hemispheric sky cover is then determined as the ratio of the cloudy pixels to the total number of pixels over the predefined FOV. The cloud decision algorithm is valid for solar elevation angles greater than 10° and ignores the 10° of sky near the horizon, giving a FOV of 160°. However, for the large FOV (e.g., 160°), cloud sides may contribute significantly to the total sky cover under partly cloudy skies. *Kassianov et al*. [2005] analyzed the differences in hemispheric cloud fraction estimates as a function of averaging time, FOV, and cloud spatial structure and found that compared to horizontally projected cloud fraction, a 15 min average of highly sampled sky cover is the minimum time span in order for the "sky cover" to best relate to nadir-projected cloud fraction. They also found that 15 min is shown to be the decorrelation time of the sky view, and averaging that long with highly sampled data can thus compensate for the individual image view distortion of the cloud elements as they move across the sky view. For the same cloud field, they found that hemispheric-view cloud fraction on average increases as FOV increases. Therefore, we use hourly 100° FOV total sky cover to represent the TSI cloud fraction. The TSI was first deployed at the ARM SGP Central Facility in July 2000; thus, no data is available prior to this time. More details about the TSI cloud fraction estimates can be found in *Morris* [2005]. Hourly TSI cloud fraction estimates from July 2000 to August 2011 from the ARMBE products are used in this study. Note that the hourly TSI cloud fraction estimates before 5 April 2005 were retrieved based on a 20° FOV zenith circle. Since the mean diurnal variation from 20° FOV before 5 April 2005 shows an average 0.02 difference (i.e., 0.001 to 0.04 difference in mean hourly cloud fractions) compared to that from a 100° FOV zenith circle after 5 April 2005 (not shown) and the difference of 0.02 is well within the uncertainty of the TSI sky cover retrievals, we include all the hourly TSI cloud fraction estimates from July 2000 to August 2011 for the long-term statistical comparisons with the assumption that the impact of the TSI zenith FOV switch is minor.

Observations from the direct and diffuse broadband shortwave (SW) radiometers deployed at the ARM SGP Central Facility are also used to estimate the sky cover. *Long and Ackerman* [2000] used the observations of surface downwelling total and diffuse SW radiation to detect daylight clear-sky time periods for an effective 160° FOV from a vertically upward pointing radiometer system. Given a statistically significant subset of detected clear-sky observations over the course of a sufficient range of solar zenith angles on given days, daily clear-sky irradiance functions are fitted, interpolated for cloudy periods, and used to produce continuous estimates of clear-sky total, direct, and diffuse irradiance. This further allows the estimation of the impact of clouds on the hemispheric radiation field. *Long et al*. [2006a] used coincident observations from broadband

radiometers and carefully screened TSI sky cover to propose a relationship between the impact of clouds on measured downwelling diffuse shortwave radiation at the surface and hemispheric sky cover within 160° FOV. In this study, we use the 15 min averages of 160° FOV fractional sky cover (cloud fraction hereafter; data source: "sgp15swfanalsirs1longC1.c1") from March 1997 to December 2011, available at http://www.arm.gov/instruments/sirs. Based on *Long et al*. [2006a], the RFA sky cover estimates agree to better than ~10% root-mean-square sky cover amount with sky imager retrievals and human observations. In a paper on evaluating representation of cloud properties for three widely used reanalyses (ERA-Interim, National Centers for Environmental Prediction (NCEP)/National Center for Atmospheric Research Reanalysis I, and NCEP/Department of Energy Reanalysis II), *Wu et al*. [2012] used the same 160° FOV RFA cloud fraction estimates and found that all of the reanalyses exhibit significant underestimation in modeling cloud fraction, surface relative shortwave cloud forcing, and cloud albedo. As you will find out later from this paper, the conclusion drawn by *Wu et al*. [2012] is well justified at least from the perspective of observed cloud fractions in general.

2.1.3. Cloud Fraction Estimates From Satellite-Based Passive Remote Sensing

The three satellite-based cloud fraction estimates (GOES, ISCCP, and PATMOS-x) used are briefly introduced below.

The GOES NASA (the National Aeronautics and Space Administration)-Langley VISST (Visible Infrared Solar-Infrared Split Window Technique) cloud fraction estimates ("GOES cloud fraction estimates" hereafter) are derived by the NASA Langley cloud and radiation group from multiple GOES passive radiometer observations, including GOES-8 (1997 to March 2003), GOES-10 (April 2003 to July 2006), and GOES-11 (August 2006). It is worth emphasizing that in this paper GOES cloud fraction estimates represent the retrieved cloud fraction product from the NASA Langley cloud and radiation group using multiple GOES passive radiometer observations and thus should not be confused with GOES satellites (e.g., GOES-8 satellite). GOES-10/11 was at 135°W whereas GOES-8 was at 75°W. Each GOES pixel (4 km spatial resolution at nadir) is classified as either clear or cloudy by comparing the observed visible (0.65 μm) reflectance, solar to infrared (3.8 to 10.8 μm) brightness temperature, and infrared brightness temperature difference to thresholds based on predicted clear-sky values [*Minnis et al*., 2008]. It is worth mentioning that viewing and solar geometry can impact cloud fraction estimates because of its impact on radiance measurements [e.g., *Evan et al*., 2007; *Kato and Marshak*, 2009], and the potential impact includes discontinuities of those retrieved cloud fractions from GOES satellites located at different geographic locations. Detailed investigation concerning instrumental calibration and its error/uncertainty can be found at http://www.oso.noaa.gov/goes/goes-calibration/index.htm. The cloud fraction is estimated as the number of cloudy pixels divided by the total number of pixels in 0.5° latitude/longitude resolution centered at the ARM SGP site (reported as averages approximately every half hour by the Minnis product). Adjacent half-hourly cloud fraction estimates are averaged into the hourly cloud fractions reported here. In order to investigate impacts of spatial scale on the retrieved cloud fraction, we use the Minnis half-hourly 0.5° product to generate hourly GOES cloud fraction over 1°, 3°, and 5° domains centered at the ARM SGP Central Facility (see Figure 2). The four sets of hourly GOES cloud fraction estimates from January 1997 to December 2011 are used in this study. Data sources are "sgpgoes8minnisX1.c1" for retrievals from 01 January 1997 to 30 April 1998, and "sgpvisstgridg*minnisX1.c1" for retrievals from 01 May 1998 to 31 December 2011, where "*" represents "08v2," "08v3," "10v2," "10v3," "11v3," "11v4," or "13v4." The GOES optical depth product of cloudy pixels from the same data sources are used to plot Figure 10.

The ISCCP cloud fraction estimates used are total cloud fractions from 3-hourly 2.5° equal-area ISCCP D1, and 3-hourly 2.5° fixed latitude/longitude ISCCP D1 and monthly 2.5° fixed latitude/longitude ISCCP D2 over the ARM SGP site from January 1997 to December 2009. The ISCCP cloud fraction estimates were generated using the infrared (~ 11 μm) and visible (~ 0.6 μm) radiances from global geostationary (primarily from three satellite series: GOES, Geostationary Meteorological Satellite (GMS), and the European Meteorological Satellite (Meteosat) and polar-orbiting (AVHRR) meteorological satellites [e.g., *Knapp*, 2008; *Rossow and Schiffer*, 1999]. Note that ISCCP D1 and D2 are retrieved primarily based on GOES measurements over the SGP site. However, the ISCCP uses a different cloud detection algorithm and different sampling strategy compared to ARMBE GOES [*Minnis et al*., 2008]. Descriptions on detection algorithms for ISCCP D-series can be found in *Rossow et al*. [1985], *Rossow and Garder* [1993], and *Rossow et al*. [1996]. The ISCCP D-series data sets have several improvements compared to their previous version (C-series), including revised radiance calibrations and reduced biases in cirrus cloud properties. The improvement in cloud detection from ISCCP C-series to ISCCP D-series includes the following: (1) improved cirrus detection over land by lowering

infrared threshold from 6 K to 4 K, (2) improved polar cloud detection over ice and snow surfaces by lowering visible threshold from 0.12 to 0.06 and by using threshold test on 3.7 m radiances, and (3) improved detection of low clouds at high latitudes by changing to visible reflectance threshold test [*Rossow et al*., 1996]. The ISCCP cloud fractions represent fractional areal cloud cover. ISCCP D1 cloud fraction is determined by pixel level observations in each grid box. ISCCP D2 is monthly average of ISCCP D1, with an adjustment of ISCCP D1 cloud amount to ISCCP D2 to account for the nighttime pixels that have no visible channel cloud detection. More detailed information about the product's algorithm, threshold, and evaluation of uncertainty can be found in *Rossow et al*. [1993]. In this study, we use 3-hourly 2.5° equal-area ISCCP D1 over the grid box centered at (97.75°W, 36.25°N) which is the closest to the central facility ("3-hourly 2.5° equal-area ISCCP D1" hereafter), and 3-hourly 5° fixed longitude/latitude ISCCP D1 ("3-hourly 5° ISCCP D1" hereafter) and monthly 5° fixed longitude/latitude ISCCP D2 ("monthly 5° ISCCP D2" hereafter) cloud fraction estimates averaged from four 3-hourly 2.5° fixed longitude/latitude ISCCP D1 and four monthly 2.5° fixed longitude/latitude ISCCP D2 cloud fraction estimates, considering that the SGP Central Facility site is located at the adjacent side of two 2.5° fixed longitude/latitude ISCCP D1 and D2 grid boxes. The 3-hourly 2.5° fixed latitude/longitude ISCCP D1 and monthly ISCCP D2 products were downloaded from http://isccp.giss.nasa.gov, and 3-hourly 2.5° equal-area ISCCP D1 product ("ISCCP.D1.*.GLOBAL.*.GPC") was downloaded from https://eosweb.larc.nasa.gov/project/isccp/isccp_d1_nat_table. The infrared cloud top-pressure data from 3-hourly 2.5° equal-area ISCCP D1 are used to plot Figure 12.

The AVHRR PATMOS-x ("PATMOS-x" hereafter) cloud fraction estimates are derived using observations from the National Oceanic and Atmospheric Administration's (NOAA's) AVHRR polar-orbiting satellites [*Stowe et al*., 2002; *Jacobowitz et al*., 2003] and more recently the European Organization for the Exploitation of Meteorological Satellites (EUMETSAT) Polar Orbiting Meteorological (METOP) satellites. AVHRR PATMOS-x is processed from Global Area Coverage data, which uses the mean of four 1.1 km AVHRR pixels selected from an area of approximately 3×5 km to represent a single pixel. A Bayesian cloud detection algorithm with six classifiers calibrated over multiple surface types is used to determine the presence of clouds in a given pixel [*Heidinger et al*., 2012]. The training data used to create the classifiers is derived from an analysis of colocated NOAA-18/AVHRR and Cloud-Aerosol Lidar and Infrared Pathfinder Satellite Observation (CALIPSO) overpasses based on cloud mask threshold. The PATMOS-x cloud fractions are estimated as the number of cloudy pixels divided by the total number of pixels over each spatial domain, with an individual pixel size of 4 km [*Evan et al*., 2008]. The PATMOS-x cloud fraction estimates consist of monthly averaged fields from all available AVHRR/2 and AVHRR/3 data from 1981 to present. For most of the record, this entails four or more daily overpasses; though in much of the 80s and early 90s, only two daily overpasses are available. We should note that, being composed of several disparate polar-orbiting satellites, the PATMOS-x record is subject to effects of satellite drift [*Foster and Heidinger*, 2013]. We are making the assumption that these effects are minimized by usage of only the later portion of the record, which has the benefits of greater sampling (more satellites) and satellites with generally slower rates of orbital drift. However, it is likely that some small portion of the difference in the PATMOS-x record relative to the others can be attributed to this effect. Details on instrumental calibration and error/uncertainty can be found in published papers [e.g., *Heidinger et al*., 2012] and at website http://climserv.ipsl.polytechnique.fr/gewexca/index-4.html. In this study, we use monthly 1° longitude/latitude PATMOS-x (version 5) cloud fraction estimates over the ARM SGP Central Facility from January 1997 to December 2009. Also included in this study are the 3° and 5° cloud fraction estimates, averaged from the 1° PATMOS-x products (see Figure 2). Data files used here are the same as those used in the Global Energy and Water cycle Experiment cloud assessment and include the"CA_PATMOSX_NOAA_0130AM," "CA_PATMOSX_NOAA_0730AM," "CA_PATMOSX_NOAA_0130PM," "CA_PATMOSX_NOAA_0730PM," and "CA_PATMOSX_NOAA_AMPM" products from January 1997 to December 2009.

2.2. Approaches

The 15 min RFA data are first averaged into hourly data. For accuracy, we use only those with four valid 15 min mean data points within 1 h; that is, we filter out those hours with less than four valid 15 min mean data points within 1 h. The valid 15 min data points refer to those with 15 min mean cloud fraction between 0 and 1 (i.e., exclude "missing" or "bad" data points).

Next, the hourly or 3-hourly cloud fractions are averaged into daily cloud fractions. In this study, for a concurrent comparison, all the products have the same hourly or 3-hourly sample volume for the average.

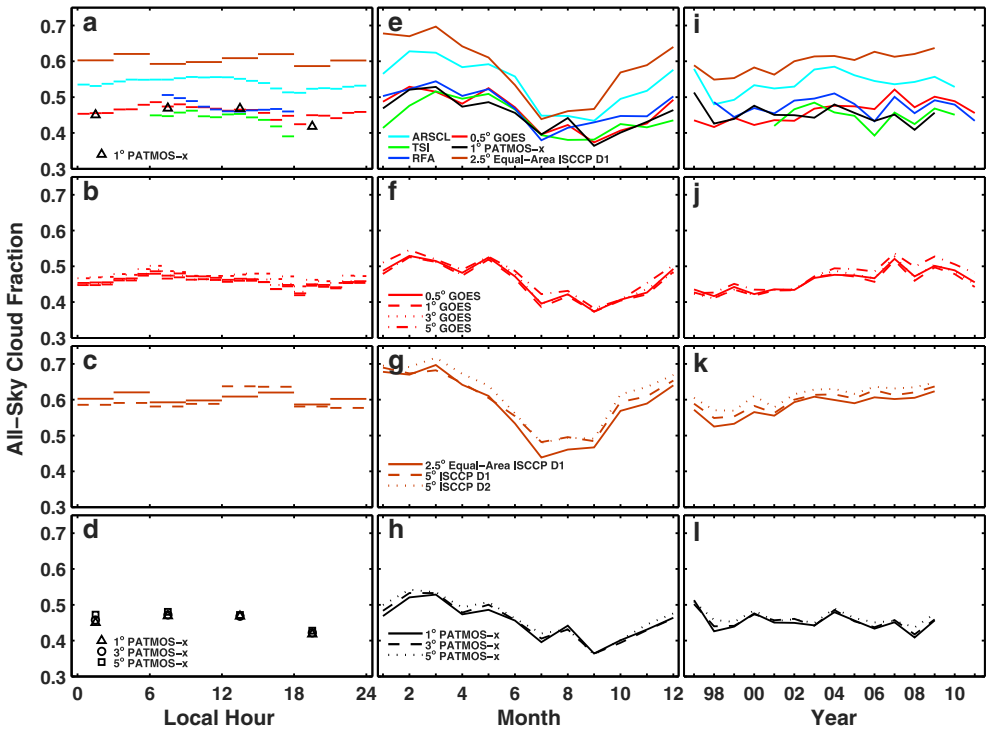

Figure 3. The 1997–2011 mean (a–d) diurnal, (e–h) annual, and (i–l) interannual variations of all-sky cloud fractions from six different ground- and satellite-based cloud fraction estimates over the ARM SGP site, Oklahoma, United States. Colors and lines: (1) the cyan lines represent ARSCL cloud fractions; (2) the green lines represent TSI cloud fractions; (3) the blue lines represent 160° FOV RFA cloud fractions; (4) the red solid, dashed, dotted, and dash-dotted lines represent GOES cloud fractions over 0.5°, 1°, 3°, and 5° latitude/longitude grid boxes, respectively; (5) the black solid, dashed, and dotted lines represent PATMOS-x cloud fractions over 1°, 3°, and 5° latitude/longitude grid boxes, respectively; (6) the brown solid, dashed, and dotted lines represent 2.5° equal-area ISCCP D1, 5° latitude/longitude ISCCP D1, and 5° latitude/longitude ISCCP D2 cloud fractions. Black triangles, circles, and squares represent mean diurnal variations from 1°, 3°, and 5° PATMOS-x cloud fractions.

However, for a comparison without concurrency, each product has its own hourly or 3-hourly sample volume for the average which includes all available valid data points. The daily cloud fractions are averaged into monthly cloud fractions and then further averaged into yearly cloud fractions. The mean diurnal, annual, and interannual variations of cloud fraction from all the estimates are then compared. Note that, "concurrent valid data point" in the comparisons refers to a data point commonly valid for all the compared estimates. To make comparisons on mean diurnal variations, a concurrent 3-hourly cloud fraction refers to a valid 3-hourly cloud fraction under the condition that within the 3-hour window, all the hourly cloud fraction estimates used in comparison have valid data points. For those cloud fraction estimates with a "flag" indicating the number of valid data points originally used in generating the estimates, including the hourly ARSCL, TSI, GOES, and 3-hourly 2.5° fixed latitude/longitude ISCCP D1, we use only those generated from more than 50% valid data points. Likewise, only those cloud vertical profiles which satisfy the condition of more than 50% lidar/ceilometer valid data points within each hour in determination of cloud base are used to generate Figure 10. Hourly or 3-hourly standard deviations are calculated for each specific hour or 3 h of a day using hourly or 3-hourly data for all the days over all the years. Monthly standard deviations are calculated for each specific month of a year using monthly data over all the years. Yearly standard deviations are calculated using monthly data for each specific year after removing mean seasonal variation, that is, the averages of monthly cloud fraction for each specific month of a year over all years.

3. Results

In this section, we compare mean diurnal, annual, and interannual variations of all-sky cloud fraction from all the estimates (without or with concurrency). Note that in this paper, unless otherwise specified, "daytime"

Table 1. Sample Statistics of 1997–2011 Monthly Cloud Fractions Over the ARM SGP Site

	Total Valid Months	Mean	Standard Deviation
ARSCL	169	0.54	0.12
TSI	133	0.44	0.12
RFA	178	0.47	0.12
0.5° GOES	180	0.46	0.11
1° GOES	180	0.46	0.11
3° GOES	180	0.46	0.11
5° GOES	180	0.47	0.10
2.5° Equal-Area ISCCP D1	156	0.58	0.12
5° ISCCP D1	156	0.60	0.11
5° ISCCP D2	156	0.61	0.11
1° PATMOS-x	156	0.45	0.11
3° PATMOS-x	156	0.46	0.10
5° PATMOS-x	156	0.46	0.09

refers to "6 A.M. to 6 P.M. local standard time (LST)" (nominal daytime), "nighttime" refers to "6 P.M. to next-day 6 A.M. LST" (nominal nighttime), "all-sky" refers to "cloud fraction ≥ 0," and "cloudy sky" refers to "cloud fraction ≥ 0.01."

3.1. Comparisons Without Concurrency

3.1.1. Mean Diurnal, Annual, and Interannual Variations of All-Sky Cloud Fractions

Figure 3 shows mean diurnal, annual, and interannual variations of all-sky cloud fractions from all the estimates. It is notable that the mean cloud fractions from ISCCP and ARSCL are much larger than those from the rest of the cloud fraction estimates (TSI, RFA, GOES, and PATMOS-x), that is, 0.15 (ISCCP) and 0.08 (ARSCL) larger in the averaged mean diurnal variations, 0.13 (ISCCP) and 0.08 (ARSCL) larger in the averaged mean annual variations, and 0.14 (ISCCP) and 0.08 (ARSCL) larger in the averaged interannual variations. In particular, the ISCCP or ARSCL mean monthly cloud fractions in January equals 0.69–0.70 or 0.56, which are 0.21–0.22 or 0.08 larger than the average (0.48) from the rest of the estimates that are similar in their overall magnitudes.

The 1997–2011 mean annual variations from ARSCL, TSI, and RFA look similar to one another and to those from 1997 to 2008 ARSCL, TSI, and RFA reported by *Qian et al*. [2012]. The 1997–2011 mean annual total cloud fraction of 53.89% from the ARMBE ARSCL is the same as the 1998–2004 ARM ARSCL mean total cloud fraction of 54% obtained by *Kollias et al*. [2007b, Table 1], similar to the 1997–2008 ARM ARSCL mean total cloud fraction of 51% obtained by *Qian et al*. [2012, Table 2] and the 1997–2010 ARM ARSCL mean total cloud fraction of 55% obtained by *Kennedy et al*. [2013, Table 5]. However, the much larger mean cloud fractions from the ARMBE ARSCL (retrieved based on radar, lidar, and laser ceilometer observations) than those from 0.5° GOES seem inconsistent with the result by *Xi et al*. [2010], where they compared 1997–2006 mean total cloud fraction (46.9%) derived from radar-lidar-*based cloud fractions* (the same instrument data streams as the ARSCL) and from 0.5° GOES over the SGP site and concluded that they have an excellent agreement. *Kennedy et al*. [2013, section 5] found the same discrepancy compared to *Xi et al*. [2010] and attributed it to the fact that *Xi et al*. [2010] used the MPL measurements only as a constraint on MMCR cloud bases. We also used current ARMBE ARSCL data and found that the 1997–2006 ARSCL mean total cloud fraction from MMCR-only measurements (i.e., the data quality flag "qc_cld_frac_source" indicates "mostly from MMCR," referring to the case that MPL was not working or did not have valid data, and MMCR had valid values, based on the ARMBE ARSCL data center) equals 47.03%, similar to the 1997–2006 radar-lidar-based mean total cloud fraction (46.9%) by *Xi et al*. [2010]. Furthermore, the mean total cloud fractions from the same product but at different temporal and spatial scales (2.5° equal-area ISCCP D1, 5° ISCCP D1 and ISCCP D2; 0.5°/1°/3°/5° GOES; 1°/3°/5° PATMOS-x) in Figure 3 show generally similar mean diurnal, annual, and interannual variations with minor (<0.05) differences. This is partially consistent with the result in *Xi et al*. [2010] that GOES's decade-long mean cloud fraction over the SGP site is insensitive to the spatial resolution from 0.5° to 2.5°.

It is worth noting that 1997–2011 ARSCL mean annual total cloud fraction from MMCR-only measurements (calculated from $>$ 50% valid points) equals 0.45, which is not far from the average of the mean annual total cloud fraction ($0.54 - 0.08 = 0.46$) from the TSI, RFA, GOES, and PATMOS-x cloud fraction estimates. In other words, the relatively large cloud fraction in ARSCL is probably associated with lidar (MPL) measurements. Also, one might expect greater consistency between PATMOS-x and ARSCL, as the PATMOS-x Bayesian cloud detection algorithm uses the CALIPSO lidar as training data. A likely cause of the difference in between is that PATMOS-x is constrained by the sensitivity of the AVHRR sensors, which may not provide sufficient radiometric contrast to detect subvisible cirrus regardless of the training data used.

Table 2. Results of Statistical Significance Based on Student *t* test and *f* test[a]

Student t Test for the Differences Between the Means of Different Monthly Cloud Fraction Estimates

	ARSCL	TSI	RFA	0.5° G	1° G	3° G	5° G	2.5° I (D1)	5° I (D1)	5° I (D2)	1° P	3° P	5° P
ARSCL	N/A	**S**	**S**	**S**	**S**	**S**	**S**	**S**	**S**	**S**	**S**	**S**	**S**
TSI	**6.91**	N/A	NS	NS	NS	NS	**S**	**S**	**S**	**S**	NS	NS	NS
RFA	**5.06**	2.31	N/A	NS	NS	NS	NS	**S**	**S**	**S**	NS	NS	NS
0.5° G	**6.24**	1.44	1.04	N/A	NS	NS	NS	**S**	**S**	**S**	NS	NS	NS
1° G	**6.67**	1.02	1.49	0.47	N/A	NS	NS	**S**	**S**	**S**	NS	NS	NS
3° G	**6.42**	1.40	1.13	0.08	0.40	N/A	NS	**S**	**S**	**S**	NS	NS	NS
5° G	**5.46**	**2.54**	0.01	1.14	1.63	1.24	N/A	**S**	**S**	**S**	NS	NS	NS
2.5° I (D1)	**3.23**	**10.08**	**8.43**	**9.74**	**10.18**	**10.00**	**9.15**	N/A	NS	NS	**S**	**S**	**S**
5° I (D1)	**4.48**	**11.68**	**9.95**	**11.40**	**11.85**	**11.71**	**10.89**	1.12	N/A	NS	**S**	**S**	**S**
5° I (D2)	**5.70**	**12.84**	**11.20**	**12.69**	**13.14**	**13.03**	**12.25**	2.35	1.30	N/A	**S**	**S**	**S**
1° P	**6.74**	0.81	1.67	0.68	0.22	0.62	1.84	**10.21**	**11.94**	**13.21**	N/A	NS	NS
3° P	**6.56**	1.08	1.41	0.40	0.07	0.33	1.57	**10.09**	**11.85**	**13.14**	0.29	N/A	NS
5° P	**6.05**	1.81	0.73	0.35	0.83	0.43	0.82	**9.71**	**11.53**	**12.87**	1.05	0.77	N/A

f Test for the Differences Between the Variances of Different Monthly Cloud Fraction Estimates

	ARSCL	TSI	RFA	0.5° G	1° G	3° G	5° G	2.5° I (D1)	5° I (D1)	5° I (D2)	1° P	3° P	5° P
ARSCL	N/A	NS	NS	NS	NS	NS	**S**	NS	NS	NS	NS	NS	**S**
TSI	1.12	N/A	NS	NS	NS	NS	NS	NS	NS	NS	NS	NS	**S**
RFA	1.10	1.01	N/A	NS	NS	NS	NS	NS	NS	NS	NS	NS	**S**
0.5° G	1.26	1.13	1.14	N/A	NS	NS	NS	NS	NS	NS	NS	NS	NS
1° G	1.26	1.13	1.14	1.00	N/A	NS	NS	NS	NS	NS	NS	NS	NS
3° G	1.36	1.22	1.24	1.08	1.08	N/A	NS	NS	NS	NS	NS	NS	NS
5° G	**1.54**	1.37	1.39	1.22	1.22	1.13	N/A	NS	NS	NS	NS	NS	NS
2.5° I (D1)	1.08	1.03	1.02	1.17	1.17	1.26	1.17	N/A	NS	NS	NS	NS	**S**
5° I (D1)	1.31	1.17	1.19	1.04	1.04	1.04	1.42	1.21	N/A	NS	NS	NS	NS
5° I (D2)	1.29	1.15	1.17	1.02	1.02	1.06	1.19	1.19	1.02	N/A	NS	NS	NS
1° P	1.38	1.23	1.25	1.10	1.10	1.01	1.11	1.28	1.06	1.07	N/A	NS	NS
3° P	1.48	1.32	1.34	1.17	1.17	1.08	1.04	1.37	1.13	1.15	1.07	N/A	NS
5° P	**1.73**	**1.55**	**1.57**	1.37	1.37	1.27	1.13	**1.60**	1.32	1.34	1.25	1.17	N/A

[a]The two-sided critical *t* value for degree of freedom great than 120 (which applies to all the cases here) at a 2% significance level is set to be the *t* value (2.36) for degree of freedom of 120. The one-sided critical *f* value for degree of freedom between 100 and 200 for both numerator and denominator (which applies to all the cases here) at a 1% significance level is set to be the mean value (1.50) of the *f* values when degree of freedoms of numerator and denominator being 100 and 100 (*f* value: 1.60), 100 and 200 (*f* value: 1.48), 200 and 100 (*f* value: 1.52), and 200 and 200 (*f* value: 1.39). Here one-sided *f* values are calculated using larger variance divided by smaller variance [*Caulcutt*, 1991]. "G," "I," and "P" represent "GOES," "ISCCP," and "PATMOS-x," respectively. "2.5° I (D1)" refers to "2.5° Equal-Area ISCCP D1." "S" or "NS" refer to "significant" or "not significant," respectively. "N/A" refers to "not apply." All the numbers representing "significant" are marked in bold.

For the mean diurnal variations, all the estimates show the smallest cloud fraction of 0.40 to 0.59 at 6 P.M. The majority of the estimates show an increase of 0.02 to 0.03 from early morning to noon and a decrease of 0.02 to 0.06 from noon to late afternoon.

For the mean annual variations, all the estimates exhibit large mean cloud fractions in winter and spring seasons, with a peak in January for 5° ISCCP D1, in February for ARSCL, GOES, and 3°/5° PATMOS-x, or in March for 2.5° equal-area ISCCP D1 and 5° ISCCP D2, 1° PATMOS-x, TSI, and RFA. The smallest mean cloud fraction is shown in summer and early fall, that is, in July for ISCCP D2 and RFA; in July and September for 2.5° equal-area and 5° ISCCP D1, in August and September for TSI; or in September for ARSCL, GOES, and PATMOS-x.

The interannual variations exhibit different tendencies: three of the estimates (from ISCCP, ARSCL, and GOES) show an overall increase of 0.08–0.10 in the annually averaged cloud fraction from 1998 to 2009; however, the other three estimates (from TSI, RFA, and PATMOS-x) exhibit little tendency of increase in the annually averaged cloud fractions in the same decade. It is worth further investigation to determine how the cloud fraction tendency links to the findings in a published paper of global brightening over the SGP [*Long et al.*, 2009]. The standard deviations of the mean cloud fractions are shown in Figure 4. As can be seen, the standard deviations of the mean hourly or 3-hourly cloud fractions range from 0.07 to 0.18. GOES shows relatively larger standard deviation near midnight, TSI and RFA show relatively larger standard deviations in the morning and afternoon, respectively, and the rest of the estimates are evenly distributed throughout the day. Note that, the GOES midnight IR calibration issue [e.g., *Yu et al.*, 2013] could be associated with the relatively larger GOES cloud fraction's standard deviation at midnight, whereas the ISCCP does not have the midnight issue (although retrieved mostly using GOES measurements over the SGP site) is probably because

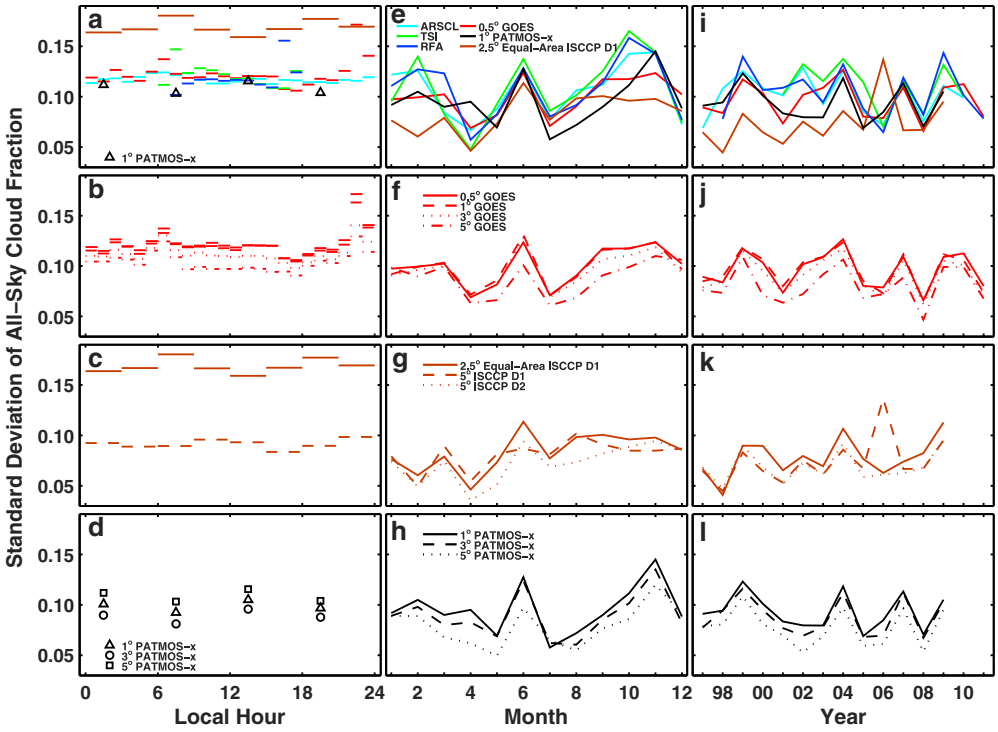

Figure 4. Standard deviations of mean cloud fractions shown in Figure 3. Colors, lines, and marks are the same as Figure 3.

ISCCP is a 3-hourly data set and does not involve the large errors associated with GOES midnight IR calibration. The standard deviations of the mean monthly cloud fractions range from 0.04 to 0.17, with the majority peaking in February, June, and October and with the smallest values in April, July, and December. For the same estimate with different spatial scales (0.5°/1°/3°/5° GOES; 1°/3°/5° PATMOS-x; 2.5° equal-area or 5° ISCCP), the standard deviations of cloud fraction over a large grid box are generally smaller than those over a small grid box, which is understandable from a statistical point of view. The only exception is the standard deviation of 5° ISCCP D1 in 2006 which shows 0.07 larger than 2.5° equal-area ISCCP D1 and 5° ISCCP D2. The standard deviations of annually averaged cloud fractions from all the estimates range from 0.04 to 0.14, varying from year to year.

3.1.2. Significance

The mean diurnal, annual, and interannual variations of cloud fractions (Figure 3) and their standard deviations (Figure 4) show large differences. Are they statistically significant? In this section, we address this question. We first examine the statistical frequency distributions of cloud fractions at different temporal and spatial scales and then test significance of the differences between the means (or variances) of different cloud fraction estimates.

Figure 5 shows the histograms (or the number of occurrence) of daily cloud fraction from all the estimates. Note that 5° ISCCP D2 and 1°/3°/5° PATMOS-x are at monthly temporal resolution and thus not included. The histograms of daily cloud fraction exhibit distributions dependent on spatial scales. Those over relatively small spatial scales (ARSCL, TSI, RFA, and 0.5°/1° GOES) show U-shaped histograms; however, the number of occurrence either increases or decreases with cloud fraction magnitude for those over relatively large spatial scales (2.5° equal-area or 5° ISCCP D1 or 3°/5° GOES). The results suggest that daily cloud fractions do not have a Gaussian distribution, and thus, the common significance tests cannot be used here.

The histograms of monthly cloud fraction from all the estimates are shown in Figure 6. All the monthly cloud fractions exhibit quasi-Gaussian distributions. The histograms from the same estimates (2.5° equal-area or 5° ISCCP D1 and 5° ISCCP D2; 0.5°/1°/3°/5° GOES; 1°/3°/5° PATMOS-x) look similar to each other. The histograms from TSI, RFA, 0.5° GOES, and 1° PATMOS-x have similar distributions, with the highest frequency of occurrence for the monthly cloud fraction from 0.40 to 0.50 and with almost no occurrence for monthly cloud fraction less than 0.10 or greater than 0.75. Note that TSI has a smaller peak value (20 times) than RFA (29 times), 0.5° GOES

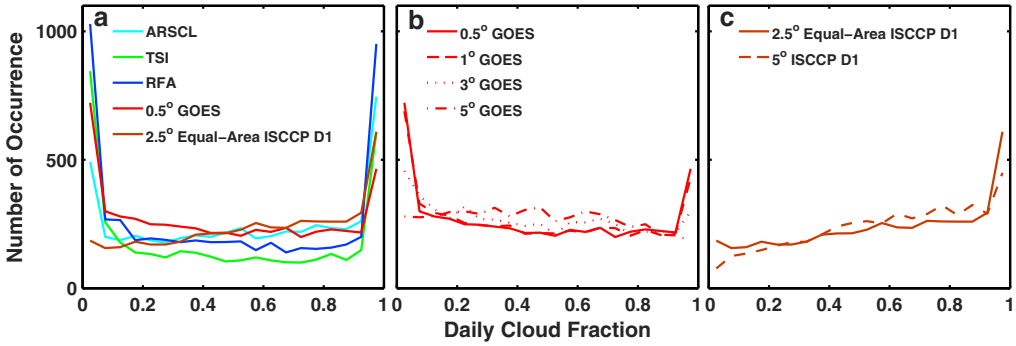

Figure 5. The histograms of 1997–2011 daily cloud fractions from all the estimates. Colors and lines are the same as in Figures 3 and 4.

(30 times) or 1° PATMOS-x (31 times), probably because TSI has fewer valid monthly cloud fractions than RFA, 0.5° GOES or 1° PATMOS-x. However, the histograms from 2.5° equal-area ISCCP D1 and ARSCL show different distributions when compared to those from the other estimates. For the monthly cloud fraction, 2.5° equal-area ISCCP D1 and ARSCL have the highest frequency of occurrence from 0.62 to 0.68 and from 0.55 to 0.60, respectively, much larger than the other estimates. The largest monthly cloud fractions from (2.5° equal-area or 5°) ISCCP and ARSCL are the same (0.82), much larger than those (0.72–0.75) from the other estimates. Likewise, the smallest monthly cloud fractions from (2.5° equal-area or 5°) ISCCP and ARSCL are 0.27–0.35 and 0.25, much larger than those (0.15–0.21) from the other estimates. Note that the U-shaped frequency distributions of daily cloud fraction and the quasi-Gaussian distributions of monthly cloud fraction from ARSCL, TSI, and RFA in general look similar to those reported by *Qian et al.* [2012], obtained from 1997 to 2008 concurrent daily and

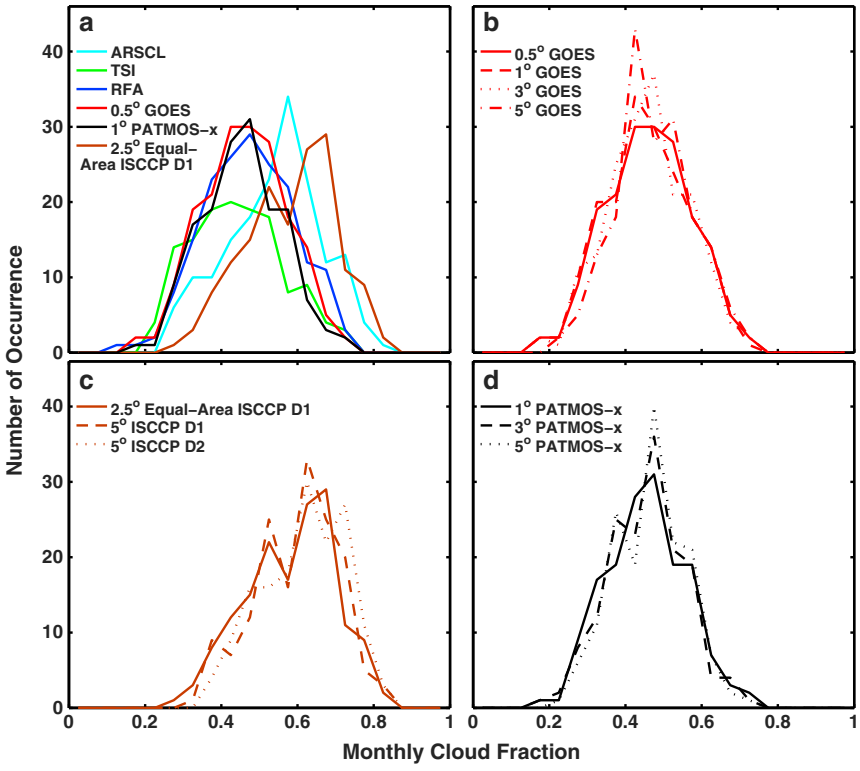

Figure 6. The histograms of 1997–2011 monthly cloud fractions from all the estimates. Colors and lines are the same as in Figures 3–5.

monthly cloud fractions. The only exception is that ARSCL daily cloud fractions with magnitude <0.10 in *Qian et al.* [2012] do not have high occurrence as shown in Figure 5.

The autospectral density distributions and autocovariance distributions of monthly cloud fraction from all the estimates are further examined (not shown). Results show that the monthly cloud fractions from TSI and RFA do not have a periodic signal (a peak at a certain frequency); the monthly cloud fractions from the other estimates include either a weak (ARSCL, GOES, and PATMOS-x) or a relatively strong (ISCCP) narrow-band signal with a frequency of 1 $year^{-1}$.

The quasi-Gaussian distributions of all the monthly cloud fractions permit an examination of significance of the differences between the means or variances from different cloud fraction estimates using Student's *t* test or *f* test. Table 1 lists sample statistics of monthly cloud fraction estimates, including valid months, means, and standard deviations which were calculated without removing mean seasonal variation. Table 2 lists the results from the statistical significance tests for monthly cloud fractions. The formulas and requirements of the significance tests can be found in a general statistical book [e.g., *Bendat and Piersol*, 1986; *Caulcutt*, 1991] and thus omitted here.

Table 2 (2) shows that at a 1% significance level (one-sided *f* test) the difference of the variances from different monthly cloud fraction estimates are not significant except for ARSCL versus 5° GOES, and 5° PATMOS-x versus ARSCL/TSI/RFA/2.5° equal-area ISCCP D1. Table 2 (1) shows that at a 2% significance level (two-sided *t* test) both ARSCL and ISCCP mean cloud fractions exhibit statistically significant differences compared to the mean cloud fractions from all the other estimates, except for 2.5° equal-area ISCCP D1 versus 5° ISCCP D1, 2.5° equal-area ISCCP D1 versus 5° ISCCP D2, and 5° ISCCP D1 versus 5° ISCCP D2. TSI mean cloud fraction also shows a statistically significant difference compared to 5° GOES mean cloud fraction. Except for the cases mentioned above, the mean cloud fractions from all the other estimates do not show a statistical significance. It is worth mentioning that if using a more permissive 5% significance level: (1) the two-sided critical *t* value will be 1.98, and thus, it does not change the results except that the two pairs (TSI versus RFA and 2.5° Equal-Area ISCCP D1 versus 5° ISCCP D2) are now determined to be significantly different; (2) the one-sided critical *f* value will be 1.33, and thus, it does not change the results except that those pairs (3° GOES versus ARSCL, 5° GOES versus TSI/RFA, 1° PATMOS-x versus ARSCL, 3° PATMOS-x versus ARSCL/RFA, 5° PATMOS-x versus 0.5°/1° GOES, and 5° PATMOS-x versus 5° ISCCP D2) are now determined to be significantly different. Overall, 5% significance level seems a too permissive threshold for this analysis.

The statistical significance of the overall increase of 0.08–0.10 in the annually averaged cloud fractions from 1998 to 2009 in three of the estimates (ISCCP, ARSCL, and GOES) is also examined using a standard procedure/method that can be found in a general statistics book [e.g., *Caulcutt*, 1991, chapter 10]. Basically, a linear regression fit was first conducted, and then Student's *t* test was applied to determine the significance of the estimated trend. For the annually averaged cloud fractions, the calculated Student's *t* values are 5.47, 6.05, 5.25, 2.48, and 4.87/4.09/4.81/5.76 for 2.5° equal-area ISCCP D1, 5° ISCCP D1, 5° ISCCP D2, ARSCL, and 0.5°/1°/3°/5° GOES, which are all greater than the critical *t* value 2.36 at a 1% significance level (one-sided *t* test) with a degree of freedom of 120. Note that the degrees of freedom for all the cases here are greater than 120, corresponding to smaller critical *t* values than those with a degree of freedom of 120. In other words, the overall increase of 0.08–0.10 from 1998 to 2009 in ISCCP, ARSCL, and GOES are significant at a 1% significance level. Of course, a more permissive 5% significance level leads to a smaller critical *t* value of 1.66 (one-sided and with a degree of freedom of 120) and thus does not change the results of significance test. Nevertheless, it is worth mentioning that decade-long annually averaged cloud fractions may not be statistically long enough to state "trend."

3.2. Comparisons With Concurrency

Based on the results shown in section 3.1, (2.5° equal-area or 5°) ISCCP and ARSCL cloud fractions are significantly larger than other estimates. Could the disagreement be caused by the different volumes of hourly or 3-hourly data points used in the comparisons? In this section, we examine this issue by using concurrent hourly and 3-hourly cloud fractions. The cloudy times from hourly or 3-hourly cloud fractions refer to the total number of hourly cloudy times or the total number of 3-hourly cloudy times.

Figure 7 shows mean diurnal, annual, and interannual variations of all-sky cloud fractions from concurrent daytime (2001–2010) or nighttime (1997–2010) all-sky hourly or 3-hourly cloud fractions. The daytime or

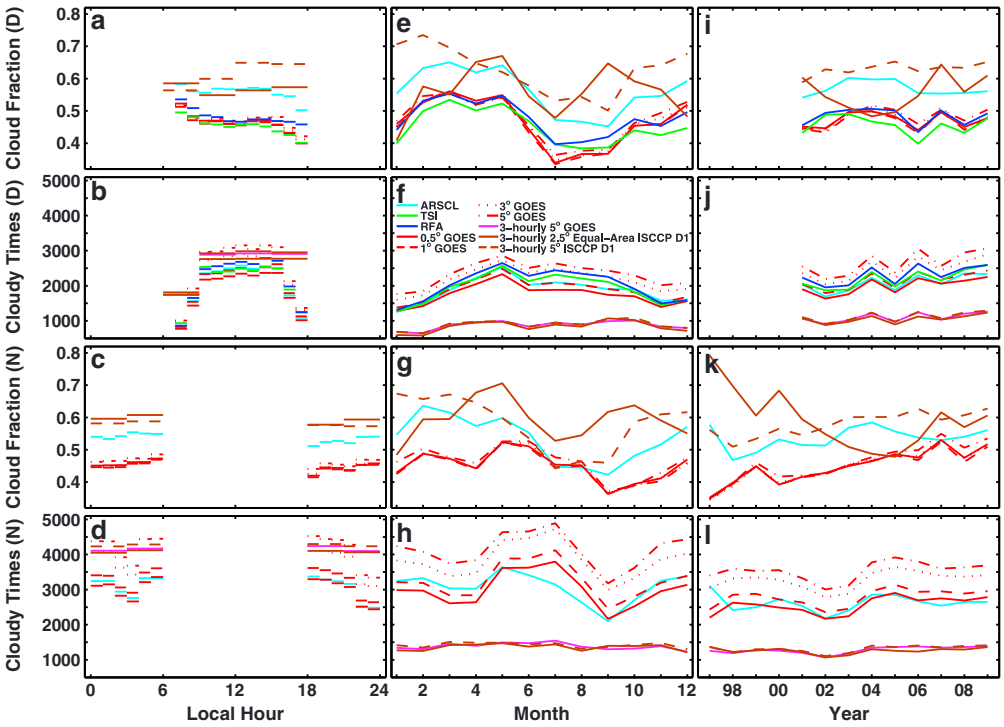

Figure 7. The 2001–2010 mean (a and b) diurnal, (e and f) annual, and (i and j) interannual variations of concurrent daytime all-sky hourly or 3-hourly cloud fractions, and 1997–2010 mean (c and d) diurnal, (g and h) annual, and (k and l) interannual variations of concurrent nighttime all-sky hourly or 3-hourly cloud fractions. Colors and lines are the same as in Figures 3–6, except that the purple lines in Figures 7b, 7d, 7f, 7h, 7j, and 7l represent 3-hourly 5° GOES cloud fractions. Note that, except for 3-hourly 5° GOES, 3-hourly 2.5° equal-area ISCCP D1, and 3-hourly 5° ISCCP D1, all the others are from hourly cloud fractions.

nighttime mean cloud fractions from 2.5° equal-area ISCCP D1, 5° ISCCP D1, and ARSCL are 0.02 to 0.30 larger than those from the rest of the estimates all day and throughout the year, except for daytime 2.5° equal-area ISCCP D1 from December to March when the mean cloud fractions from 2.5° equal-area ISCCP D1 and TSI/RFA/GOES are comparable, and except for nighttime 5° ISCCP D1 and ARSCL from June to August when the mean cloud fractions from 5° ISCCP D1 and ARSCL are comparable to those from 0.5°/1°/3°/5° GOES. In particular, 5° ISCCP D1 or ARSCL daytime mean monthly cloud fraction in January equals 0.71 or 0.55, which is 0.26 or 0.10 larger than the average (0.45) from TSI, RFA, and 0.5°/1°/3°/5° GOES. In January, 5° ISCCP or ARSCL nighttime mean monthly cloud fraction equals 0.67 or 0.55, which is 0.24 or 0.11 larger than the average (0.43) of all the other estimates (0.5°/1°/3°/5° GOES). Both daytime and nighttime 2.5° equal-area ISCCP D1 cloud fractions are smaller than the corresponding 5° ISCCP D1 from December to March. Daytime mean diurnal cloud fractions from 2.5° equal-area ISCCP D1 is 0.05 to 0.09 smaller than those from 5° ISCCP D1 from 9 A.M. to 6 P.M. Daytime mean monthly cloud fractions from 2.5° equal-area ISCCP D1 are comparable to 5° ISCCP D1 from April to October except that in September, the former is 0.13 larger than the latter, and in November, the former is 0.09 smaller than the latter. Nighttime 2.5° equal-area ISCCP D1 cloud fractions from April to October are 0.02 to 0.14 larger than 5° ISCCP D1 cloud fractions, and in November, their cloud fractions are comparable. Nighttime 2.5° equal-area ISCCP D1 and 5° ISCCP D1 have a comparable magnitude in their mean 3-hourly cloud fractions. As expected, the annually averaged cloud fractions from 2.5° equal-area ISCCP D1, 5° ISCCP D1, and ARSCL are much larger than those from the rest of the estimates, except for daytime 2.5° equal-area ISCCP D1 from 2003 to 2005, nighttime 2.5° equal-area ISCCP D1 in 2004 and 2005, and nighttime ARSCL in 2007 that show similar cloud fractions to those from the rest of the estimates. It is worth mentioning that there is a large difference between the concurrent mean cloud fractions from 3-hourly 2.5° equal-area ISCCP D1 and from 3-hourly 5° ISCCP D1. Different geographical sizes might be one cause, considering of geographical significance of cloud inhomogeneity which we do not see from 0.5°/1°/3°/5° GOES data sets.

The mean diurnal, annual, and interannual variations of daytime all-sky cloud fraction from 0.5°/1°/3°/5° GOES, TSI, and RFA are close to each other, with differences no more than 0.08; however, the total numbers of

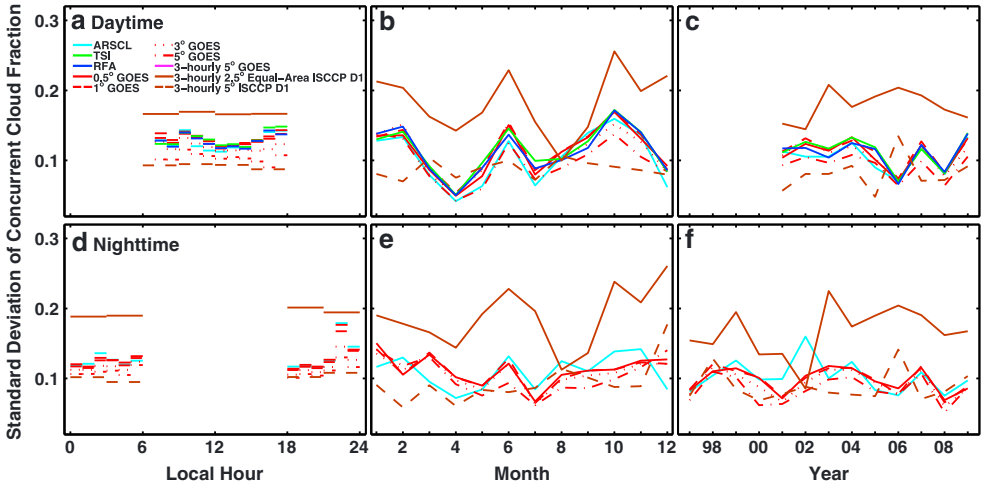

Figure 8. Standard deviations of mean cloud fractions shown in Figure 7. Colors and lines are the same as Figures 3–7.

their cloudy times can differ largely. For example, for the daytime case, 0.5° GOES has no more than 0.07 difference in the 2001–2010 mean monthly cloud fractions from TSI and RFA, but its hourly cloudy times in a month (for example, 1885 times in July) can differ largely compared to those from TSI (2319 times in July) and RFA (2442 times in July). In other words, the relatively small differences in the 2001–2010 daytime mean monthly cloud fractions do not indicate a good agreement on daytime hourly cloud fraction time series. Likewise, the mean annual variations of nighttime all-sky cloud fraction from 0.5°/1°/3°/5° GOES are close to each other, with difference no more than 0.04. For both daytime and nighttime cases, the mean diurnal, annual, and interannual variations of 0.5°/1°/3°/5° GOES cloud fractions are close to each other (with difference no more than 0.02 for the daytime case and no more than 0.04 for the nighttime case), similar to Figure 3. The GOES cloudy times averaged over a large spatial scale are larger than those over a small spatial scale, which is not a surprise because a cloud must exist over a large spatial area if a cloud exists over a small spatial area inside the large area but the opposite is not true. As can be seen from Figure 7, the difference in nighttime cloudy times are larger than that in daytime cloudy times, and 3-hourly 2.5° equal-area ISCCP D1, 5° ISCCP D1, and 5° GOES have a good agreement in their daytime and nighttime cloudy times. Overall, the majority of the estimates show the largest frequency of daytime clouds in May and relatively low frequency of daytime clouds from November to February, and the least nighttime cloudy times in September and relatively large nighttime cloudy times from May to July.

The corresponding standard deviations of the concurrent mean cloud fractions are shown in Figure 8. The majority of the standard deviations range from 0.04 to 0.17, peaking in June, October, and December that are probably linked to relatively large standard deviations in late afternoon and near midnight. In general, the 2.5° equal-area ISCCP D1 has larger standard deviations when compared against that of the other estimates, the exceptions being in August and September.

4. Discussions

Section 3 shows that there exists a substantial disagreement between different cloud fraction estimates. In particular, ARSCL and ISCCP monthly mean cloud fractions show statistically significant differences compared to those from the rest of the estimates based on a two-sided *t* test at a 2% significance level. This section briefly discusses some potential issues relevant to the large differences.

The contour pairs in Figure 9 show the joint frequency distributions of concurrent daytime hourly cloud fractions. The majority of the hourly cloud fractions from all the estimates are basically divided into two populations: cloud fractions greater than 0.80 or less than 0.20, consistent with the U-shaped frequency distribution previously reported by *Hogan et al.* [2001], although there are notable differences in the details. The majority of hourly ARSCL cloud fractions are either greater than 0.90 or less than 0.20. For a large portion of the ARSCL cloud fractions that are $>$0.90, the corresponding TSI, RFA, or 0.5° GOES cloud fractions exhibit

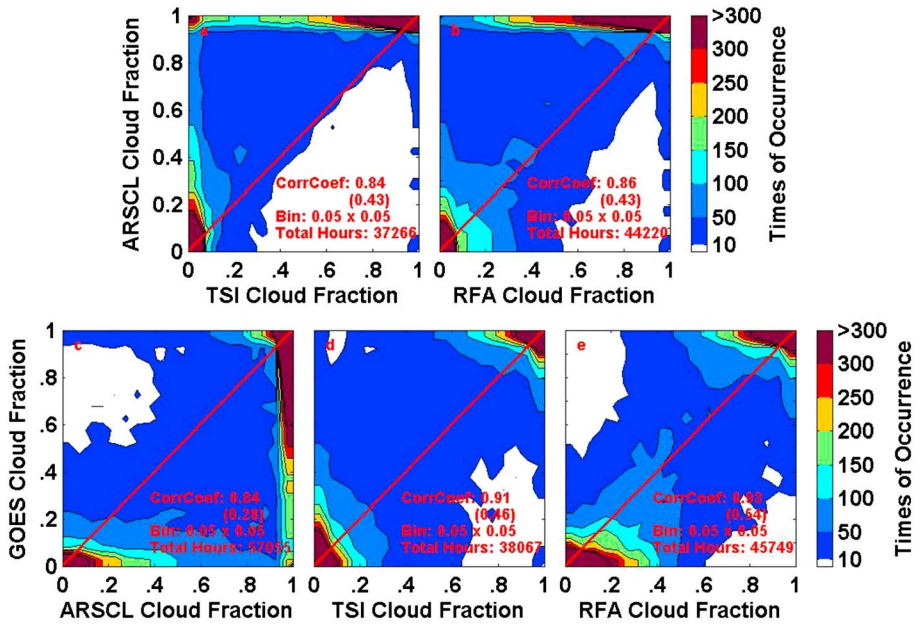

Figure 9. Joint frequency distributions of concurrent daytime all-sky hourly cloud fractions ((a and b) ARSCL versus TSI/RFA and (c–e) 0.5° GOES versus ARSCL/TSI/RFA). In each panel, a red diagonal line represents a perfect match as a reference, and a correlation coefficient is shown on the bottom right corner. The correlation coefficients without a parenthesis are from all-sky cloud fractions, and those with a parenthesis are from cloud fractions from 0.10 to 0.90.

any value between 0 and 1, mostly falling into two ranges ($<$0.05 or $>$0.50) for TSI, $>$0.35 for RFA, and $>$0.45 for 0.5° GOES. For a large portion of ARSCL cloud fractions that are $<$0.20, the corresponding TSI, RFA, or 0.5° GOES cloud fractions are mostly $<$0.10. In other words, ARSCL has a large portion of large ($>$0.90) or small ($<$0.20) hourly cloud fractions that are greater than the corresponding TSI, RFA, or 0.5° GOES hourly cloud fractions. TSI or RFA hourly cloud fraction estimates have a relatively good agreement with 0.5° GOES hourly cloud fraction estimates with the majority of the data points gathering around the diagonal line.

The differences of the cloud fractions between ARSCL and the other estimates shown in Figure 9 are at least in part because ARSCL cloud fractions are retrieved based on active sensors which can effectively detect high and optically thin cirrus clouds that are not traditionally considered as cloudy sky while TSI, RFA, and 0.5° GOES cloud fractions are all retrieved from passive instruments that categorize high subvisual to translucent cirrus clouds using a more traditional "clear-sky" definition [*Dupont et al*., 2008]. To illustrate the contribution of these thin cirrus clouds, Figure 10a shows a comparison of cloud fraction estimates from ARSCL and GOES for all the cases where the lowest cloud base as determined from ARSCL is greater than 6 km (here defined as cirrus clouds). ARSCL almost always shows a larger cloud fraction than GOES. To further support the influence of thin cirrus on the ARSCL cloud fraction, Figures 10b to 10d compare 1999–2009 cloud fraction estimates from ARSCL and GOES for all the daytime cases (Figure 10b) where the lowest cloud base as determined from ARSCL is greater than 6 km, and then subdivide Figure 10b into cases where the GOES visible optical depth is greater than three (Figure 10c) and less than three (Figure 10d). Note that the optical depth values are for cloudy sky only, and so, the 0.5° grid box optical depth refers to the mean optical depth for cloudy pixels within the grid box. These figures show that for cases of optically thick cirrus, the ARSCL and GOES cloud fractions agree much better in the aggregate average, while for the optically thin cirrus, ARSCL shows a consistently larger cloud fraction. This is consistent with the statement by *Zhao et al*. [2012] or *Stubenrauch et al*. [2013] that the differences in cloud macrophysical properties (cloud fraction here) are rooted in the differences in the instrument basis, retrieval methods, and the errors and biases in the measurement inputs. Furthermore, in Figure 9, the correlation coefficients in all the contour pairs are higher than 0.84 for all-sky cloud fractions but less than 0.54 for cloud fractions from 0.10 to 0.90. It suggests that all the daytime hourly cloud fractions have a relatively good agreement in their phase variations, but the high correlations between the daytime hourly cloud fractions are driven by the large portion of the near clear-sky ($<$0.10) and near overcast (0.90) occurrences.

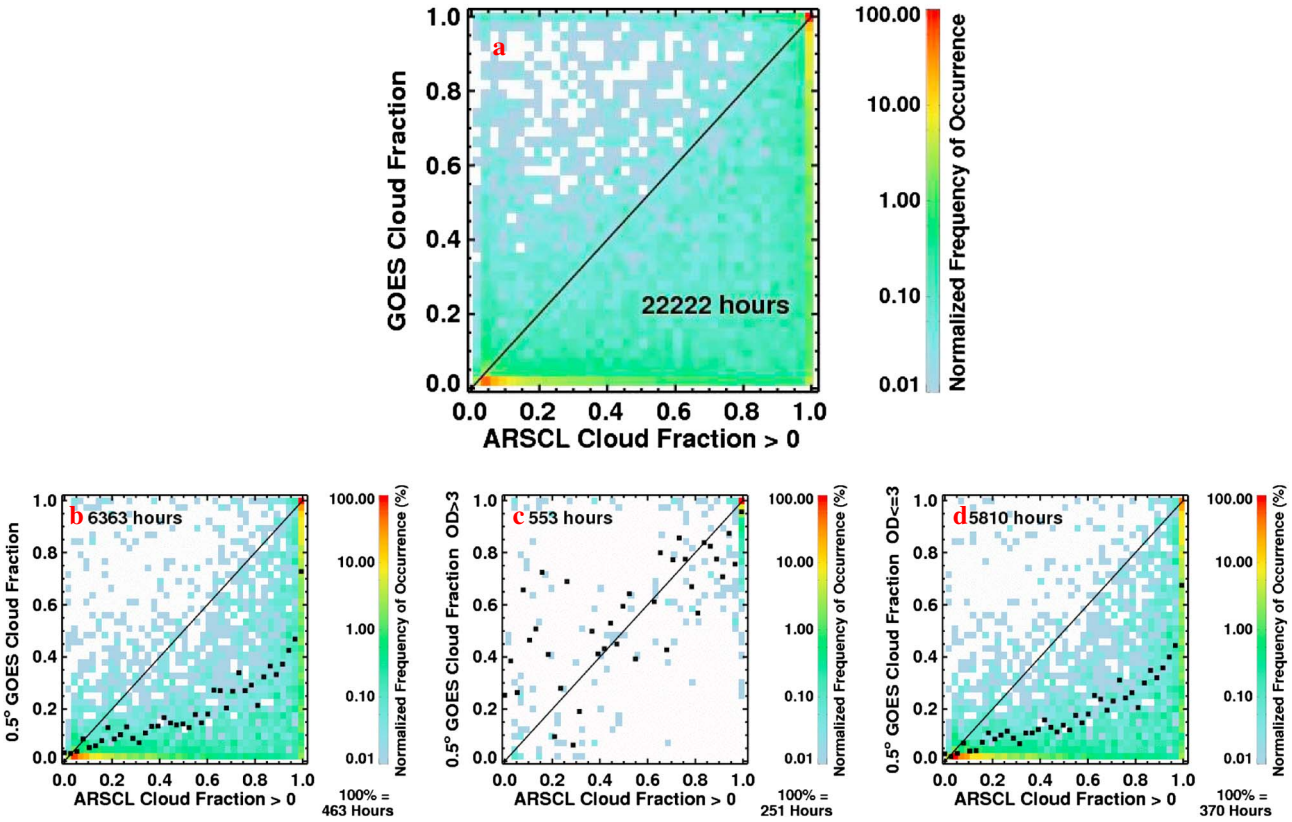

Figure 10. (a) Normalized frequency of occurrence of concurrent hourly ARSCL cloud fraction and hourly 0.5° GOES cloud fraction for all the cases from 1997 to 2011, where ARSCL shows the lowest cloud base at greater than 6 km (here defined as cirrus clouds). Normalized frequency of occurrence of concurrent hourly ARSCL cloud fractions and hourly 0.5° GOES cloud fractions for daytime cases from 1999 to 2009 with solar zenith angle less than 75°, where ARSCL shows the lowest cloud base for the entire hour at greater than 6 km for (b) all the cases, (c) GOES optical depth of cloudy pixels greater than 3, and (d) GOES optical depth of cloudy pixels less than or equal to 3. Small black squares indicate the mean hourly 0.5° GOES cloud fraction per ARSCL cloud fraction bin of 0.025. For the cases of comparatively optically thicker clouds in Figure 10c, we see good agreement of hourly total cloud fraction between ARSCL and GOES. However, for the optically thinner cases in Figure 10d, ARSCL shows much larger hourly total cloud fraction than GOES. Total hours are written in each panel.

The contour pair of nighttime hourly cloud fractions between 0.5° GOES and ARSCL exhibits a similar pattern as that of their daytime hourly cloud fractions and thus is not shown.

The contour pairs from 3-hourly 5° GOES and 5° ISCCP D1 cloud fractions are shown in Figure 11. Like the hourly cloud fractions in Figure 9, the majority of the 3-hourly cloud fractions are separated into two populations: greater than 0.80 or less than 0.20. The majority of the 3-hourly 5° ISCCP D1 cloud fractions are much larger than the 3-hourly 5° GOES cloud fractions. For large ($>$0.90) 3-hourly 5° ISCCP D1 cloud fractions, the corresponding 3-hourly 5° GOES cloud fractions exhibit any values between 0 to 1, mostly falling into two ranges ($>$0.60 or $<$0.10). In other words, 5° ISCCP D1 has a large portion of large ($>$0.90) 3-hourly cloud fractions that are greater than 5° GOES. Because both 5° ISCCP D1 and 5° GOES are satellite-based observations, the cases with 3-hourly 5° GOES $<$ 0.10 and 3-hourly 5° ISCCP D1 $>$ 0.90 are difficult to understand. By further looking into the data, those cases occurring in the nighttime period (total 605 cases) are more than double the number of cases occurring in the daytime period (total 265 cases). It is worth reminding that daytime here refers to "nominal daytime (6 A.M. to 6 P.M. LST)," and nighttime refers to "nominal nighttime (6 P.M. to next-day 6 A.M. LST)." For both daytime and nighttime cases, the mismatches (with 3-hourly 5° GOES $<$ 0.10 and 3-hourly 5° ISCCP D1 $>$ 0.90) occur much less frequently from May to September than in other months. This indicates that the 3-hourly 5° ISCCP D1 cloud fractions are much larger than the 3-hourly 5° GOES cloud fractions, especially from October to the following April. Further investigation is needed to find out whether the difficulty to distinguish cloud and snow could be one factor to make the difference in retrieved satellite-based cloud fractions during this period of time. Note that

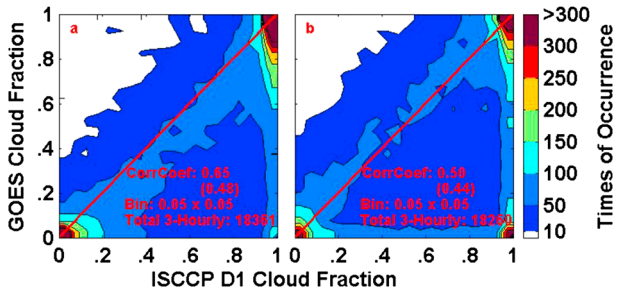

Figure 11. Joint frequency distribution of concurrent daytime ("nominal daytime", 6 am to 6 pm LST) (a) and nighttime ("nominal nighttime", 6 pm to next-day 6 am LST) (b) all-sky 3-hourly cloud fractions (5^{O} GOES vs 5^{O} ISCCP D1). In each panel, a red diagonal line represents a perfect match as a reference, and a correlation coefficient is shown on the bottom right corner. The correlation coefficients without a parenthesis are from all-sky cloud fractions, and those with a parenthesis are from cloud fractions from 0.10 to 0.90.

ISCCP uses a visible and infrared threshold during the daytime and then determines a secondary infrared-only threshold to match the visible and infrared cloud amount during the daytime. This secondary infrared-only threshold is then applied for nighttime to obtain consistent cloud amount. However, the GOES approach uses multiple infrared channel thresholds for nighttime.

The correlation coefficients in the 3-hourly contour pairs are low (0.65 or 0.50 for all-sky daytime or nighttime 3-hourly 5° cloud fractions, and 0.48 or 0.44 for daytime or nighttime 3-hourly 5° cloud fractions from 0.10 to 0.90), further suggesting that the 3-hourly 5° ISCCP D1 and the 3-hourly 5° GOES cloud fractions have a poor agreement in their phase variations.

To illustrate the contribution to the difference of total cloud fraction between GOES and ISCCP, Figures 12a and 12b show a comparison of daytime/nighttime 3-hourly 2.5° equal-area ISCCP D1 and 3-hourly 2.5° GOES (taken over the same area as the ISCCP grid box) confirming that ISCCP cloud fractions are generally larger than GOES. Like the case for 5° ISCCP D1 and 5° GOES (Figure 11), 2.5° equal-area ISCCP D1 shows a large portion of large ($>$0.90) 3-hourly cloud fractions that are greater than 2.5° GOES which is mostly falling into two ranges ($>$0.80 or $<$0.10). By further partitioning into cases of predominantly high clouds (c and d) and predominantly low clouds (e and f), it can be seen that ISCCP and GOES agree relatively well on average for predominantly high clouds, but for predominantly low clouds ISCCP shows a much larger cloud fraction in general. Note that, "high cloud" is defined as that for which ISCCP infrared cloud top pressure is less than or equal to 440 mbar, as defined by ISCCP. Conversely, "low cloud" is defined as that for which ISCCP infrared cloud top pressure is greater than 440 mbar. "Predominantly high clouds" means that in the ISCCP profile of cloud fraction, there is at least double the amount of clouds at high levels (infrared cloud top pressure $<=$ 440 mbar) as there are at low levels (infrared cloud top pressure $>$ 440 mbar). Likewise, "Predominantly low clouds" means that in the ISCCP profile of cloud fraction, there is at least double the amount of clouds at low levels (infrared cloud top pressure $>$ 440 mbar) as there are at high levels (infrared cloud top pressure $<=$ 440 mbar). It is worth mentioning that we tested the sensitivity to the low clouds defined by ISCCP cloud top-pressure threshold and found little impact on our results; some (perhaps even many) scenes may include thin cirrus despite ISCCP cloud top-pressure $>$ 440 mbar.

The first step toward investigating the larger cloud fractions reported by ISCCP compared to GOES was to look for differences between the nominal daytime (6 A.M. to 6 P.M. LST) and nominal nighttime (6 P.M. to next-day 6 A.M. LST) periods (Figures 11 and 12). For this application, we defined the split between daytime (solar zenith angle (SZA) $<$ 75°) and nighttime (SZA $>$ 100°) so that more precisely taking into account seasonal variations in the length of the day. This analysis showed that the relationship between 3-hourly 2.5° equal-area ISCCP and 3-hourly 2.5° GOES cloud fractions for the SZA-based daytime case looks similar to that for the SZA-based nighttime case with a small difference in between (not shown).

Figure 13 shows an example to illustrate the differences in detecting and defining cloud fractions. On 17 December 2007 between approximately 1330 and 1800 UTC, the MMCR detects a thin layer of cirrus cloud between 8 km and 10 km (Figure 13a). From the Eulerian view of the MMCR, the observed cloud is virtually unbroken and the resulting ARSCL cloud fraction is 1 (or nearly so) over this entire period. Coincident images from the TSI at 1424 UTC (Figure 13b) and 1731 UTC (Figure 13d) clearly indicate the presence of optically thin cirrus clouds that still exhibit a significant blue tint for the sky oriented in streaks (likely contrails). However, the TSI cloud decision algorithm (see section 2.1.2) results (Figures 13c and 13e)

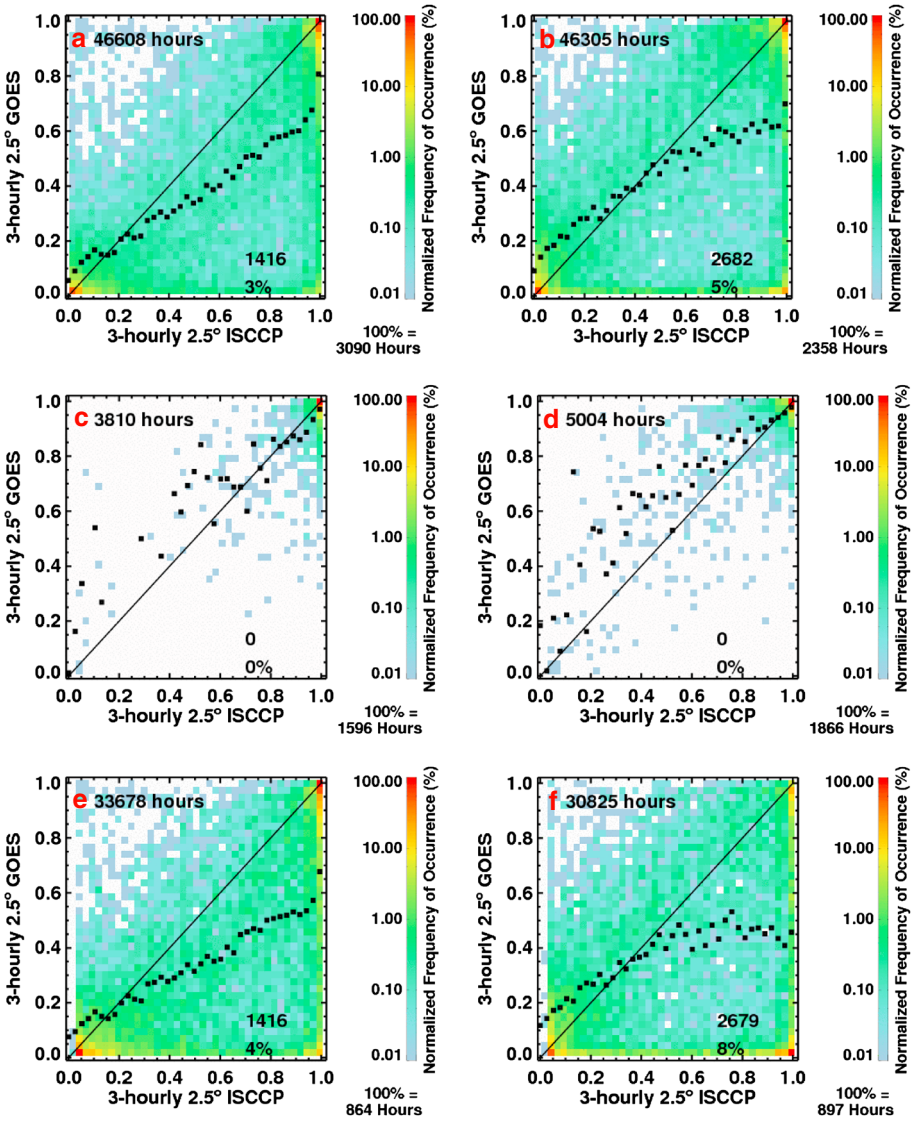

Figure 12. Normalized frequency of occurrence of concurrent 3-hourly 2.5° GOES cloud fractions and 3-hourly equal-area 2.5° ISCCP D1 cloud fractions over the same area with a center at (97.75°W, 36.25°N) from 1999 to 2009. Cases: all (a) daytime and (b) nighttime cases; (c) daytime and (d) nighttime cases with predominantly high clouds for which there is at least twice the amount of high cloud as low cloud, that is, total cloud fraction (high cloud) $>=2\times$ total cloud fraction (low cloud); and (e) daytime and (f) nighttime cases with predominantly low clouds for which there is at least twice the amount of low cloud as high cloud, that is, total cloud fraction (low cloud) $>=2\times$ total cloud fraction (high cloud). Here "high cloud" is defined as that for which infrared cloud top pressure is less than or equal to 440 mbar, as defined by ISCCP. Conversely, "low cloud" is defined as that for which infrared cloud top pressure is greater than 440 mbar. Small black squares indicate the mean 3-hourly 2.5° GOES total cloud fraction per 3-hourly equal-area 2.5° ISCCP D1 total cloud fraction bin of 0.025. In each panel, the total hours (called "A") are written in upper left corner, the total hours where the ISCCP total cloud fraction >0.90 and the GOES total cloud fraction <0.10 (called "B") are written in bottom right corner, and the percentage in bottom right corner refers to B/A. Note that in this figure, daytime and nighttime refer to 6 A.M. to 6 P.M. local standard time (LST) ("nominal daytime") and 6 P.M. to next-day 6 A.M. LST ("nominal nighttime") as in Figure 11.

indicate that these thin cirrus clouds are below the set threshold, and therefore, the cloud fractions estimated from the TSI are 0.01 for a 100° FOV and 0.06 for a 160° FOV at 1424 UTC, and 0.07 for a 100° FOV and 0.18 for a 160° FOV at 1731 UTC. In this case, and for many of the other large discrepancies, a combination of cloud orientation and morphology, instrument viewing geometry and FOVs, and differences in classification thresholds results in large differences in cloud fraction estimates and makes the determination of a "best estimate" difficult.

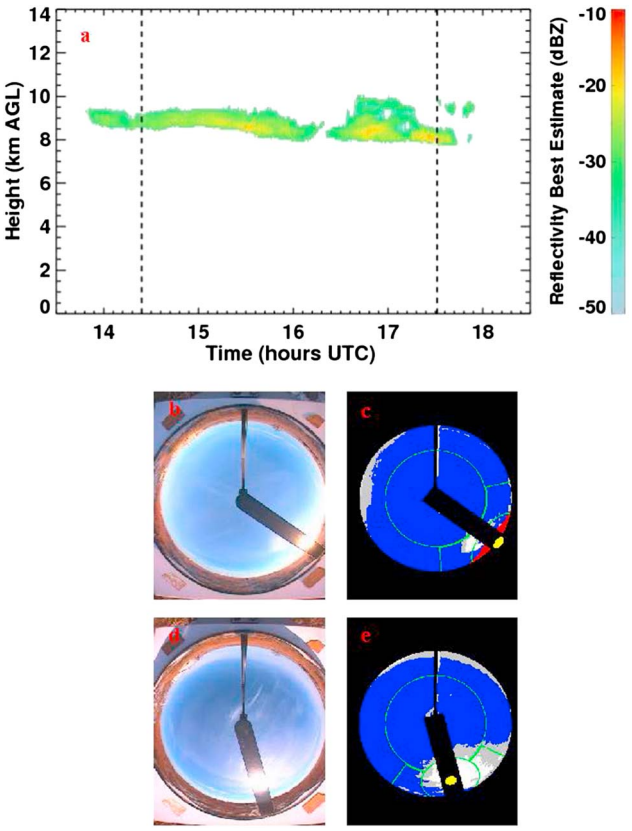

Figure 13. An example of cloud observations for December 17, 2007 illustrating a typical case where large discrepancies exist between cloud fraction estimates. (a) ARSCL best estimate radar reflectivity showing cloud fraction 1 at 1424 UTC or 1731 UTC (the dashed lines), where "AGL" refers to "Above Ground Level", (b) TSI true color image at 1424 UTC, (c) TSI cloud identification at 1424 UTC (cloud fraction = 0.01 for a 100° FOV or 0.06 for a 160° FOV), (d) TSI true color image at 1731 UTC, and (e) TSI cloud identification at 1731 UTC (cloud fraction = 0.07 for a 100° FOV or 0.18 for a 160° FOV). The inner circle and the whole circle represent a 100° FOV and a 160° FOV, respectively.

5. Summary

This study compares multiscale mean cloud fractions based on 1997–2011 observationally based cloud fraction estimates from six different platforms over the ARM SGP sites. Three ground-based estimates (ARSCL, TSI, and RFA) and three satellite-based estimates (GOES, ISCCP, and PATMOS-x) at multiple temporal and spatial scales are examined. Large differences of cloud fraction between different estimates are found. In particular, ISCCP and ARSCL are found to have significantly larger cloud fractions than the rest of the estimates. Three estimates (ISCCP, ARSCL, and GOES) exhibit an overall increase of 0.08–0.10 in the annually averaged cloud fractions from 1998 to 2009; however, the other three estimates (TSI, RFA, and PATMOS-x) exhibit little tendency of cloudiness increase in the same decade. Furthermore, daily cloud fractions exhibit frequency distributions dependent on spatial scales, which are different from monthly cloud fractions showing quasi-Gaussian frequency distributions.

It should be recognized, as already discussed by *Stephens* [1988] and *Wiscombe* [2005], that cloud fraction is often determined by a threshold of radiation properties, which in turn is likely dependent on wavelength. As discussed above, the determination of cloud fraction also depends on many other factors including cloud orientation and morphology, and instrumental viewing geometry and FOVs. Thus, different observationally based cloud fraction estimates may be best for addressing specific issues. For example, ARSCL has a certain advantage in studying vertical distributions of cloud fraction compared to all other estimates. It is worth mentioning that although ISCCP exhibits much larger total cloud fractions than GOES and PATMOS-x over the SGP site as shown in this paper, the latitudinal variation of total cloud fraction from ISCCP agrees well with those from 10 other satellite-based total cloud fractions including PATMOS-x [*Stubenrauch et al*., 2013, Figure 2]. Nevertheless, the existing large differences between cloud fraction estimates suggest a need for further investigation into the causes underlying the large differences pertaining to the observationally based cloud fraction estimates being used in any particular research endeavor. For practical purposes, it is important to use a consistent definition of cloud fraction in both climate models and observations, since inconsistent definitions of cloud fraction may end up with completely different conclusions as shown in this study. At the very minimum, any activity that professes to produce a value for cloud fraction should also give some valuation of what limit is used to delineate between cloud and no cloud.

It is also worth emphasizing that the development of consistent and accurate cloud fraction estimates as well as other cloud properties (e.g., optical thickness) is crucial for climate studies, especially from the perspective of the Earth's radiation budget. As shown in *Koren et al*. [2007], even a "twilight zone," a belt around currently classified clouds (with a width of 10 km or more) forming and evaporating cloud fragments and hydrated

aerosols, can significantly impact the estimation of the Earth's radiative forcing. In other words, computing cloud fraction and associated cloud properties over both cloud edges and interior is important for determining the Earth's radiation budget. Of course, because the determination of cloud fraction is dependent on many factors (e.g., wavelength, instrumental viewing geometry and FOVs, etc.), a "cloud-free" atmosphere must be dependent on those factors as well and so does a twilight zone. For making a better estimation of the Earth's radiation budget in a cloudy atmosphere, it is necessary to separately investigate cloudy atmosphere, the twilight zone, and cloud-free atmosphere, as pointed out by *Koren et al*. [2007] and *Bar-Or et al*. [2010, 2011]. Further studies are highly suggested on how to consistently define and determine cloudy atmosphere, the twilight zone, and cloud-free atmosphere in climate models and observations for better estimating the Earth's radiation budget.

Acknowledgments

This work has been supported by the Office of Biological and Environmental Research of the U.S. Department of Energy as part of the Earth System Modeling program via the Fast-physics System Testbed and Research (FASTER) project (www.bnl.gov/faster), Atmospheric Radiation Measurement program, and Atmospheric Systems Research program, the National Climatic Data Center, and the Brookhaven National Laboratory Laboratory Directed Research and Development Program. Recognition is also extended to those responsible for the operation and maintenance of the instruments that produced the data used in this study; their diligent and dedicated efforts are often underappreciated. We thank Peter H. Daum for carefully reading and editing the manuscript and providing constructive comments, Alan K. Betts, William B. Rossow, Warren J. Wiscombe, and Stephen E. Schwartz for helpful comments and suggestions. We also thank Wuyin Lin, Karen Johnson, Shaocheng Xie, Renata B. McCoy, Mandana Khaiyer, Violeta Golea, and Victor R. Morris for assistance on cloud fraction products used in this study.

References

Ackerman, T. P., and G. M. Stokes (2003), The atmospheric radiation measurement program, *Phys. Today*, *56*, 38–44, doi:10.1063/1.1554135.

Ackerman, S. A., R. E. Holz, R. Frey, E. W. Eloranta, B. C. Maddux, and M. McGill (2008), Cloud detection with MODIS Part II: Validation, *J. Atmos. Oceanic Technol.*, *25*, 1073–1086.

Ahlgrimm, M., and M. Köhler (2010), Evaluation of trade cumulus in the ECMWF model with observations from CALIPSO, *Mon. Weather Rev.*, *138*, 3071–3083.

Barker, H. W., G. L. Stephens, and Q. Fu (1999), The sensitivity of domain-averaged solar fluxes to assumptions about cloud geometry, *Q. J. R. Meteorol. Soc.*, *125*, 2127–2152.

Bar-Or, R. Z., I. Koren, and O. Altaratz (2010), Estimating cloud field coverage using morphological analysis, *Environ. Res. Lett.*, *5*, 014022, doi:10.1088/1748-9326/5/1/014022.

Bar-Or, R. Z., O. Altaratz, and I. Koren (2011), Global analysis of cloud field coverage and radiative properties, using morphological methods and MODIS observations, *Atmos. Chem. Phys.*, *11*, 191–200, doi:10.5194/acp-11-191-2011.

Bedacht, E., S. K. Gulev, and A. Macke (2007), Intercomparison of global cloud cover fields over oceans from the VOS observations and NCEP/NCAR reanalysis, *Int. J. Climatol.*, *27*, 1707–1719.

Bendat, J. S., and A. G. Piersol (1986), *Random Data Analysis and Measurement Procedures*, 2nd ed., 566 pp., John Wiley, New York.

Bender, F. A.-M. (2011), Planetary albedo in strongly forced climate, as simulated by the CMIP3 models, *Theor. Appl. Climatol.*, *105*, 529–535, doi:10.1007/s00704-011-0411-2.

Bouniol, D., et al. (2010), Using continuous ground-based radar and lidar measurements for evaluating the representation of clouds in four operational models, *J. Appl. Meteorol. Climatol.*, *49*, 1971–1991.

Brooks, M. E., R. J. Hogan, and A. J. Illingworth (2005), Parameterizing the difference in cloud fraction defined by area and by volume as observed with radar and lidar, *J. Atmos. Sci.*, *62*, 2248–2260.

Caulcutt, R. (1991), *Statistics in Research and Development*, 2nd ed., 471 pp., Chapman & Hall, U. K.

Clothiaux, E. E., T. P. Ackerman, G. G. Mace, K. P. Moran, R. T. Marchand, M. A. Miller, and B. E. Martner (2000), Objective determination of cloud heights and radar reflectivities using a combination of active remote sensors at the ARM CART sites, *J. Appl. Meteorol.*, *39*, 645–665, doi:10.1175/1520-0450(2000)039<0645:ODOCHA>2.0.CO;2.

Del Genio, A. D., M.-S. Yao, W. Kovari, and K. K. Lo (1996), A prognostic cloud water parameterization for global climate models, *J. Clim.*, *9*, 270–304, doi:10.1175/1520-0442(1996)009<0270:APCWPF>2.0.CO;2.

Di Girolamo, L., and R. Davies (1997), Cloud fraction errors caused by finite resolution measurements, *J. Geophys. Res.*, *102*, 1739–1756, doi:10.1029/96JD02663.

Dupont, J. C., M. Haeffelin, and C. N. Long (2008), Evaluation of cloudless-sky periods detected by shortwave and longwave algorithms using lidar measurements, *Geophys. Res. Lett.*, *35*, L10815, doi:10.1029/2008GL033658.

Evan, A. T., A. K. Heidinger, and D. J. Vimont (2007), Arguments against a physical long-term trend in global ISCCP cloud amounts, *Geophys. Res. Lett.*, *34*, L04701, doi:10.1029/2006GL028083.

Evan, A. T., A. K. Heidinger, and Y. Liu (2008), State of the climate in 2007, *Bull. Am. Meteorol. Soc.*, *89*, S23–S26.

Foster, M. J., and A. K. Heidinger (2013), PATMOS-x: Results from a diurnally corrected thirty-year satellite cloud climatology, *J. Clim.*, *26*, 414–425, doi:10.1175/JCLI-D-11-00666.1.

Guichard, F., D. B. Parsons, J. Dudhia, and J. Bresch (2003), Evaluating mesoscale model predictions of clouds and radiation with SGP ARM data over a seasonal timescale, *Mon. Weather Rev.*, *131*, 926–944.

Heidinger, A., A. T. Evan, M. J. Foster, and A. Walther (2012), A naive Bayesian cloud-detection scheme derived from CALIPSO and applied within PATMOS-x, *J. Appl. Meteorol. Climatol.*, *51*, 1129–1144.

Hogan, R. J., and A. J. Illingworth (2000), Deriving cloud overlap statistics from radar, *Q. J. R. Meteorol. Soc.*, *126*, 2903–2909.

Hogan, R. J., C. Jakob, and A. J. Illingworth (2001), Comparison of ECMWF winter-season cloud fraction with radar-derived values, *J. Appl. Meteorol.*, *40*, 513–525.

Jacobowitz, H., L. L. Stowe, G. Ohring, A. Heidinger, K. Knapp, and N. R. Nalli (2003), The Advanced Very High Resolution Radiometer Pathfinder Atmosphere (PATMOS) climate dataset: A resource for climate research, *Bull. Am. Meteorol. Soc.*, *84*, 785–793, doi:10.1175/BAMS-84-6-785.

Jakob, C. (1999), Cloud cover in the ECMWF reanalysis, *J. Clim.*, *12*, 947–959.

Kassianov, E., C. N. Long, and M. Ovtchinnikov (2005), Cloud sky cover versus cloud fraction: Whole-sky simulations and observations, *J. Appl. Meteorol.*, *44*, 86–98, doi:10.1175/JAM-2184.1.

Kato, S., and A. Marshak (2009), Solar zenith and viewing geometry-dependent errors in satellite retrieved cloud optical thickness: Marine stratocumulus case, *J. Geophys. Res.*, *114*, D01202, doi:10.1029/2008JD010579.

Kennedy, A. D., X. Dong, B. Xi, S. Xie, Y. Zhang, and J. Chen (2011), A comparison of MERRA and NARR reanalyses with the DOE ARM SGP data, *J. Clim.*, *24*, 4541–4557, doi:10.1175/2011JCLI3978.1.

Kennedy, A. D., X. Dong, and B. Xi (2013), Cloud fraction at the ARM SGP site: Instrument and sampling considerations from 14 years of ARSCL, *Theor. Appl. Climatol.*, doi:10.1007/s00704-013-0853-9.

Knapp, K. R. (2008), Calibration assessment of ISCCP geostationary infrared observations using HIRS, *J. Atmos. Oceanic Technol.*, *25*, 183–195.

Kollias, P., E. E. Clothiaux, B. A. Albrecht, M. A. Miller, K. P. Moran, and K. L. Johnson (2005), The atmospheric radiation measurement program cloud profiling radars. An evaluation of signal processing and sampling strategies, *J. Atmos. Oceanic Technol.*, *22*, 930–948, doi:10.1175/JTECH1749.

Kollias, P., E. E. Clothiaux, M. A. Miller, E. P. Luke, K. L. Johnson, K. P. Moran, K. B. Widener, and B. A. Albrecht (2007a), The atmospheric radiation measurement program cloud profiling radars: Second-generation sampling strategies, processing and cloud data products, *J. Atmos. Sci.*, *24*, doi:10.1175/JTECH2033.1.

Kollias, P., G. Tselioudis, and B. A. Albrecht (2007b), Cloud climatology at the Southern Great Plains and the layer structure, drizzle, and atmospheric modes of continental stratus, *J. Geophys. Res.*, *112*, D09116, doi:10.1029/2006JD007307.

Koren, I., L. A. Remer, Y. J. Kaufman, Y. Rudich, and J. V. Martins (2007), On the twilight zone between clouds and aerosols, *Geophys. Res. Lett.*, *34*, L08805, doi:10.1029/2007GL029253.

Liu, Y., W. Wu, M. P. Jensen, and T. Toto (2011), Relationship between cloud radiative forcing, cloud fraction and cloud albedo, and new ground-based approach for determining cloud albedo, *Atmos. Chem. Phys.*, *11*, 7155–7170, doi:10.5194/acp-11-7155-2011.

Loeb, N. G., B. A. Wielicki, F. G. Rose, and D. R. Doelling (2007), Variability in global top-of-atmosphere shortwave radiation between 2000 and 2005, *Geophys. Res. Lett.*, *34*, L03704, doi:10.1029/2006GL028196.

Long, C. N. (2010), Correcting for circumsolar and near-horizon errors in sky cover retrievals from sky images, *Open Atmos. Sci. J.*, *4*, 45–52.

Long, C. N., and T. P. Ackerman (2000), Identification of clear skies from broadband pyranometer measurements and calculation of downwelling shortwave cloud effects, *J. Geophys. Res.*, *105*(D12), 15,609–15,626.

Long, C. N., D. W. Slater, and T. Tooman (2001), Total sky imager model 880 status and testing results. ARM Technical Report ARM TR-006, U.S. Department of Energy, Washington, D. C.

Long, C. N., T. P. Ackerman, K. L. Gaustad, and J. N. S. Cole (2006a), Estimation of fractional sky cover from broadband shortwave radiometer measurements, *J. Geophys. Res.*, *111*, D11204, doi:10.1029/2005JD006475.

Long, C. N., J. M. Sabburg, J. Calbo, and D. Pages (2006b), Retrieving cloud characteristics from ground-based daytime color all-sky images, *J. Atmos. Oceanic Technol.*, *23*, 633–652.

Long, C. N., E. G. Dutton, J. A. Augustine, W. Wiscombe, M. Wild, S. A. McFarlane, and C. J. Flynn (2009), Significant decadal brightening of downwelling shortwave in the continental US, *J. Geophys. Res.*, *114*, D00D06, doi:10.1029/2008JD011263.

Mace, G. G., and S. Benson-Troth (2002), Cloud layer overlap characteristics derived from long-term cloud radar data, *J. Clim.*, *15*, 2505–2515.

Manabe, S., and R. F. Strickler (1964), Thermal equilibrium of the atmosphere with a convective adjustment, *J. Atmos. Sci.*, *21*, 361–385, doi:10.1175/1520-0469(1964)021<0361:TEOTAW>2.0.CO;2.

Min, Q., T. Wang, C. N. Long, and M. Duan (2008), Estimating fractional sky cover from spectral measurements, *J. Geophys. Res.*, *113*, D20208, doi:10.1029/2008JD010278.

Minnis, P. (1989), Viewing zenith angle dependence of cloudiness determined from coincident GOES East and GOES West data, *J. Geophys. Res.*, *94*, 2303–2320, doi:10.1029/JD094iD02p02303.

Minnis, P., et al. (2008), Cloud detection in non-polar regions from CERES using TRMM VIRS and Terra and Aqua MODIS data, *IEEE Trans. Geosci. Remote Sens.*, *46*, 3857–3884.

Moran, K. P., B. E. Martner, M. J. Post, R. A. Kropfli, D. C. Welsh, and K. B. Widener (1998), An unattended cloud-profiling radar for use in climate research, *Bull. Am. Meteorol. Soc.*, *79*, 443–455, doi:10.1175/15200477(1998)079<0443:AUCPRF>2.0.CO:2.

Morris, V. R. (2005), Total Sky Imager (TSI) handbook, ARM TR-017, June 2005. [Available at http://www.arm.gov/publications/tech_reports/handbooks/tsi_handbook.pdf.]

Park, S., and C. S. Bretherton (2009), The University of Washington shallow convection and moist turbulence schemes and their impact on climate simulations with the community atmosphere model, *J. Clim.*, *22*, 3449–3469, doi:10.1175/2008JCLI2557.1.

Qian, Y., C. N. Long, H. Wang, J. M. Comstock, S. A. McFarlane, and S. Xie (2012), Evaluation of cloud fraction and its radiative effect simulated by IPCC AR4 global models against ARM surface observations, *Atmos. Chem. Phys.*, *12*, 1785–1810, doi:10.5194/acp-12-1785-2012.

Ramanathan, V., and J. A. Coakley Jr. (1978), Climate modeling through radiative-convective models, *Rev. Geophys.*, *16*, 465–489, doi:10.1029/RG016i004p00465.

Rossow, W. B., and L. C. Garder (1993), Validation of ISCCP cloud detections, *J. Clim.*, *6*, 2370–2393.

Rossow, W. B., and R. A. Schiffer (1999), Advances in understanding clouds from ISCCP, *Bull. Am. Meteorol. Soc.*, *11*, 2261–2287.

Rossow, W. B., et al. (1985), ISCCP cloud algorithm intercomparison, *J. Climate Appl. Meteorol.*, *24*, 877–903.

Rossow, W. B., A. W. Walker, and L. C. Garder (1993), Comparison of ISCCP and other cloud amounts, *J. Clim.*, *6*, 2394–2418.

Rossow, W. B., A. W. Walker, D. Beuschel, and M. Roiter (1996), International Satellite Cloud Climatology Project (ISCCP) documentation of new cloud datasets, WMO/TD-No. 737, World Meteorological Organization, 115 pp.

Slingo, A., R. C. Wilderspin, and R. N. B. Smith (1989), Effect of improved physical parameterizations on simulations of cloudiness and the Earth's radiation budget, *J. Geophys. Res.*, *94*, 2281–2301, doi:10.1029/JD094iD02p02281.

Smith, R. N. B. (1990), A scheme for predicting layer clouds and their water content in a general circulation model, *Q. J. R. Meteorol. Soc.*, *116*, 435–460, doi:10.1002/qj.49711649210.

Sokolov, A. P., and E. Monier (2012), Changing the climate sensitivity of an atmospheric general circulation model through cloud radiative adjustment, *J. Clim.*, *25*, 6567–6584, doi:10.1175/JCLI-D-11-00590.1.

Spinhurne, J. D. (1993), Micro pulse lidar, *IEEE Trans. Geosci. Remote Sens.*, *31*, 48–55.

Stephens, G. L. (1988), Radiative transfer through arbitrary shaped optical media, II: Group theory and simple closures, *J. Atmos. Sci.*, *45*, 1837–1848.

Stokes, G. M., and S. E. Schwartz (1994), The Atmospheric Radiation Measurement (ARM) program: Programmatic background and design of the cloud and radiation test bed, *Bull. Am. Meteorol. Soc.*, *75*, 1201–1221.

Stowe, L. L., H. Jacobowitz, G. Ohring, K. R. Knapp, and N. R. Nalli (2002), The Advanced Very High Resolution Radiometer (AVHRR) Pathfinder Atmosphere (PATMOS) climate dataset: Initial analyses and evaluations, *J. Clim.*, *15*, 1243–1260.

Stubenrauch, C., et al. (2013), Assessment of global cloud datasets from satellites: Project and database initiated by the GEWEX Radiation Panel, *Bull. Am. Meteorol. Soc.*, *94*, 1031–1049, doi:10.1175/BAMS-D-12-00117.

Sundqvist, H., E. Berge, and J. E. Kristjánsson (1989), Condensation and cloud parameterization studies with a mesoscale numerical weather prediction model, *Mon. Weather Rev.*, *117*, 1641–1657, doi:10.1175/1520-0493(1989)117<1641:CACPSW>2.0.CO;2.

Tiedtke, M. (1993), Representation of clouds in large-scale models, *Mon. Weather Rev.*, *121*, 3040–3061, doi:10.1175/1520-0493(1993)121<3040:ROCILS>2.0.CO;2.

Turner, D. D., S. A. Clough, J. C. Liljegren, E. E. Clothiaux, K. Cady-Pereira, and K. L. Gaustad (2007), Retrieving liquid water path and precipitable water vapor from Atmospheric Radiation Measurement (ARM) microwave radiometers, *IEEE Trans. Geosci. Remote Sens.*, *45*, 3680–3690, doi:10.1109/TGRS.2007.903703.

Walsh, J. E., W. L. Chapman, and D. H. Portis (2009), Arctic cloud fraction and radiative fluxes in atmospheric reanalyses, *J. Clim.*, *22*, 2316–2334, doi:10.1175/2008JCLI2213.1.

Warren, S. G., R. M. Eastman, and C. J. Hahn (2007), A survey of changes in cloud cover and cloud types over land from surface observations, 1971–96, *J. Clim.*, *20*, 717–738, doi:10.1175/JCLI4031.1.

Wielicki, B. A., and L. Parker (1992), On the determination of cloud cover from satellite sensors: The effect of sensor spatial resolution, *J. Geophys. Res.*, *97*, 12,799–12,823, doi:10.1029/92JD01061.

Wielicki, B. A., et al. (2002), Evidence for large decadal variability in the tropical mean radiative energy budget, *Science*, *295*, 841, doi:10.1126/science.1065837.

Wilkinson, J. M., R. J. Hogan, A. J. Illingworth, and A. Benedetti (2008), Use of a lidar forward model for global comparisons of cloud fraction between the *ICESat* lidar and the ECMWF model, *Mon. Weather Rev.*, *136*, 3742–3759.

Wiscombe, W. J. (2005), *Part I (1) (Pages 3 to 92) in 3D Radiative Transfer in Cloudy Atmospheres*, edited by A. Marshak and A. B. Davis, pp. 686, Springer, New York.

Wu, W., Y. Liu, and A. K. Betts (2012), Observationally based evaluation of NWP reanalyses in modeling cloud properties over the Southern Great Plains, *J. Geophys. Res.*, *117*, D12202, doi:10.1029/2011JD016971.

Xi, B., X. Dong, P. Minnis, and M. M. Khaiyer (2010), A 10 year climatology of cloud fraction and vertical distribution derived from both surface and GOES observations over the DOE ARM SPG site, *J. Geophys. Res.*, *115*, D12124, doi:10.1029/2009JD012800.

Xie, S., et al. (2010), CLOUDS AND MORE: ARM climate modeling best estimate data, *Bull. Am. Meteorol. Soc.*, *91*, 13–20, doi:10.1175/2009BAMS2891.1.

Xie, S., X. Liu, C. Zhao, and Y. Zhang (2013), Sensitivity of CAM5-simulated Arctic clouds and radiation to ice nucleation parameterization, *J. Clim.*, *26*, 5981–5999.

Yi, H. Y., P. Minnis, L. Nguyen, and D. R. Doelling (2001), A proposed multiangle satellite dataset using GEO, LEO and TRIANA, paper presented at 11th Conference on Satellite Meteorology and Oceanography (570-573), Am. Meteorol. Soc., Madison, Wisconsin, 12–16 Oct. [Available at http://www-pm.larc.nasa.gov/triana/documents/helen_ams2001.pdf.]

Yu, F., X. Wu, M. K. R. V. Raja, Y. Li, L. Wang, and M. D. Goldberg (2013), Diurnal and scan angle variations in the calibration of GOES imager infrared channels, *IEEE Trans. Geosci. Remote Sens.*, 51(1), Jan. 2013. [Available at http://ieeexplore.ieee.org/stamp/stamp.jsp?tp=&arnumber=6215039.]

Zhao, C., et al. (2012), Toward understanding of differences in current cloud retrievals of ARM ground-based measurements, *J. Geophys. Res.*, *117*, D10206, doi:10.1029/2011JD016792.

Zuidema, P., and D. L. Hartmann (1995), Satellite determination of stratus cloud microphysical properties, *J. Clim.*, *8*, 1638–1656, doi:10.1175/1520-0442(1995)008<1638:SDOSCM>2.0.CO;2.